Fragile X Mental Retardation Protein regulates R-loop formation and prevents global chromosome fragility

Arijita Chakraborty[1], Piroon Jenjaroenpun[2,7], Andrew McCulley[1], Jing Li[1], Sami El Hilali[3,4], Brian Haarer[1], Elizabeth A. Hoffman[1,8], Aimee Belak[5,9], Audrey Thorland[5], Heidi Hehnly[5], Chun-long Chen[3,4], Vladimir A. Kuznetsov[2,6], and Wenyi Feng[1,‡].

[1]Department of Biochemistry and Molecular Biology, SUNY Upstate Medical Univeristy, 750 East Adams Street, Syracuse, NY 13210, USA

[2]Bioinformatics Institute, Agency for Science Technology and Research (A*STAR), 30 Biopolis Street, #07-01 Matrix, Singapore 138671

[3]Institut Curie, PSL Research University, CNRS, UMR3244, F-75005 Paris, France

[4]Sorbonne Université, F-75005 Paris, France

[5]Department of Biology, Syracuse University, Syracuse, NY 13210, USA

[6]Department of Urology, SUNY Upstate Medical University, 750 East Adams Street, Syracuse, NY 13210, USA

[7]Current address: Department of Biomedical Informatics, University of Arkansas for Medical Sciences, Little Rock, Arkansas 72205, USA

[8]Current address: Department of Biochemistry and Molecular Genetics, University of Virginia Health Systems, Charlottesville, VA 22908, USA

[9]Current address: University of Maryland School of Medicine, 655 W. Baltimore Street, Baltimore MD 21201, USA

*Correspondence to: fengw@upstate.edu

ABSTRCT

Fragile X syndrome (FXS) is the most prevalent inherited intellectual disability caused by mutations in the Fragile X Mental Retardation gene (*FMR1*) and deficiency of its product, FMRP. FMRP is a predominantly cytoplasmic protein thought to bind specific mRNA targets and regulate protein translation. Its potential role in the nucleus is not well understood. We are interested in the global impact on chromosome stability due to FMRP loss. Here we report that compared to an FMRP-proficient normal cell line, cells derived from FXS patients exhibit increased chromosome breaks upon DNA replication stress induced by a DNA polymerase inhibitor, aphidicolin. Moreover, cells from FXS individuals fail to protect genomic regions containing R-loops (co-transcriptional DNA:RNA hybrids) from aphidicolin-induced chromosome breaks. We demonstrate that FMRP is important for abating R-loop accumulation during transcription, particularly in the context of head-on collision with a replication fork, and thereby preventing chromosome breakage. By identifying those FMRP-bound chromosomal loci with overlapping R-loops and fragile sites, we report a list of novel FMRP target loci, many of which have been implicated in neurological disorders. We show that cells from FXS patients have reduced expression of xenobiotics metabolic enzymes, suggesting defective xenobiotics metabolism/excretion might contribute to disease development. Our study provides new insights into the etiological basis of, and enables the discovery of new therapeutic targets for, the FXS.

KEYWORDS

Fragile X syndrome, *FMR1*, FMRP, R-loop, chromosome fragile sites, genome instability

INTRODUCTION

Fragile X syndrome (FXS) is responsible for the most common form of inherited intellectual disability and autism (Santoro et al., 2012). In most patients, FXS is caused by the $(CGG)_n$ trinucleotide repeat expansion in the 5'-untranslated region of the Fragile X Mental Retardation (*FMR1*) gene located on Xq27.3, resulting in chromosome fragility at this locus, transcriptional silencing and loss of function of the gene product, FMRP (Coffee et al., 2002; Fu et al., 1991; Krawczun et al., 1985; Pieretti et al., 1991; Verkerk et al., 1991). FXS can also manifest as a result of mutations in the FMRP coding sequence, highlighting FMRP's importance for the etiological basis for FXS (Ciaccio et al., 2017).

FMRP is an RNA binding protein and is estimated to bind ~4% of the mRNAs in the brain and regulate their translation (Ashley et al., 1993). It is becoming increasingly clear that FMRP has multi-faceted functions. The best understood cellular function of FMRP is a translational repressor in the metabotropic glutamate receptor (mGluR)-mediated long-term depression (LTD) (Bear et al., 2004). The absence of FMRP permits increased level of protein synthesis at postsynaptic dendrites and prolonged LTD, which are normally inhibited by mGluR activation, thus causing many of the symptoms of FXS (Bear et al., 2004; Darnell et al., 2011; Nakamoto et al., 2007; Niere et al., 2012). Genome-wide studies have identified over 6,000 FMRP-interacting mRNAs, many of which are involved in synaptic signaling and function (Ashley et al., 1993; Brown et al., 2001; Darnell et al., 2011). However, only a small percentage of these putative FMRP targets have been validated by independent methods (Sethna et al., 2014) and mGluR antagonist drugs have yet to show efficacy in human patients despite preclinical success in animal models. A recent study also uncovered a translational enhancing role of FMRP towards large autism-associated genes (Greenblatt and Spradling, 2018). Thus, it stands to reason that additional key FMRP targets that meet therapeutic potential remain at large. Consistent with its role as a translation repressor, FMRP is predominantly located in the cytoplasm and associates with the polysomes (Darnell et al., 2011; Khandjian et al., 2004). However, a recent study also demonstrated a chromatin-dependent role of FMRP in DNA damage response (Alpatov et al., 2014).

In this study we set out to compare replication stress-induced chromosome breaks in lymphoblastoid cell lines derived from an individual with a full mutation at *FMR1* and an

unaffected control and test the hypothesis that FMRP plays an important role in the maintenance of genome integrity. Lymphoblastoid cells have been used to reveal genetic basis for a range of neurological disorders including FXS (Brown et al., 2001). Using this system, we demonstrate that the FX genome has increased susceptibility to chromosome breakage induced by replication stress, particularly at R-loop forming sites (RLFSs), where the RNA transcript hybridizes to homologous DNA on the chromosome, yielding a DNA:RNA hybrid and a displaced DNA single strand. Despite their many roles in normal cellular functions, R-loops can initiate conflicts between transcription and replication by creating a barrier to replication fork progression, causing chromosome breakage (Garcia-Rubio et al., 2018; Hamperl et al., 2017). We present evidence that FMRP is a genome maintenance protein that prevents chromosome breakage by mediating R-loop accumulation, possibly through direct interaction with the gene substrates that are prone to R-loop formation during transcription and further enhanced by replication stress.

RESULTS

Fragile X cells show elevated DNA damage under replication stress. We chose lymphoblastoid cells derived from a Fragile X individual (GM03200, henceforth "FX"), and an unaffected control individual (GM06990, henceforth "NM"). The GM03200 cell line contains a full mutation of 570 CGG repeats at *FMR1* (Hayward et al., 2016). We analyzed genome instability in these cells by partially inhibiting replication with aphidicolin (APH, a DNA polymerase inhibitor) and causing a 10-20% increase of cells in S phase (Fig. 1A). Both cell lines showed dose-dependent increase of chromosome breaks upon APH treatment, evidenced by γH2A.X expression (a marker for DNA double strand breaks) using flow cytometric sorting (Fig. 1B) or fluorescence microscopy (Fig. 1C&D). Compared to NM cells, FX cells demonstrated at least two-fold increase of APH-induced γH2A.X expression (Fig. 1B). Notably FX cells also showed more APH-induced γH2A.X foci per nucleus than NM cells did (Fig. 1C&D). These observations suggested that the absence of FMRP causes heightened susceptibility of FX cells to replication stress by APH. These results established that the FX genome is more prone to DNA damage upon replication stress than the normal genome, thus prompting further investigation into the nature of genome instability in the FX cells. Here we adapted Break-seq, a powerful technology we first developed in yeast (Hoffman et al., 2015), to the mammalian system and mapped genome-wide chromosome breaks in untreated cells and cells treated with APH or with equal volume of the vehicle, dimenthyl sulfoxide (DMSO) (Fig. 2A). Break-seq data quality check and control experiments are described in Supplemental Information and shown in Supplemental Table S1 and Supplemental Fig. S1. For each strain/treatment combination, *e.g.*, "FX_0.03 μM APH", *consensus DSBs* from at least two replicate experiments, regardless of the total number of replicates, were derived (Supplemental Table S2). The DSBs from 0.03 μM and 0.3 μM APH-treated samples were further pooled into a composite dataset of "APH-treated DSBs", for each cell line, followed by comparison with the DMSO-treated control to identify DSBs shared by DMSO- and APH-treatment as well as those specific to each treatment (Supplemental Fig. S2A&B, Supplemental Table S2).

FX cells show global increase of DSB formation and abnormal response to drug treatment. In all experiments, FX cells produced 2-2.5 fold more DSBs than NM cells with or without drugs (Fig. 2B), consistent with high levels of DNA damage observed in FX cells by flow cytometry.

The X chromosome showed the highest density of DSBs in FX cells (Fig. 2C). Overall, there was a higher concordance of DSBs in NM cells than FX cells: while 78% of the DSBs in untreated NM cells were also present in the DMSO-treated NM cells, there was only an 8% concordance between untreated and DMSO-treated FX cells (Fig. 2B). This was unlikely an artifact because 1) the vast majority of DSBs (83%) in untreated NM cells were also identified in untreated FX cells (Supplemental Fig. S2C); and 2) 67% of the DSBs found in DMSO-treated FX cells were also identified in APH-treated FX cells (Fig. 2B). Overall, 83%, 16% and 62% of DSBs in the untreated, DMSO-treated, and dual-treated NM cells, respectively, were found in the corresponding treatments of FX cells (Supplemental Fig. S2C). We concluded the following. First, spontaneous DSBs were largely concordant between NM and FX cells. Second, spontaneous DSBs in NM cells remained in DMSO treatment, whereas FX cells "reprogrammed" DSBs in response to DMSO, suggesting unique chemical-genetic interactions in drug-treated FX cells, as subsequent analysis would reveal. Third, the dual treatment with DMSO and APH both enhanced existent DSBs (from DMSO treatment alone) and induced new DSBs, in both cell types.

DSBs are correlated with late replication timing or drug-induced transcription. Approximately 30 to 40% of DSBs in all samples occurred in genic regions with a dominant presence in the introns. In NM cells genic association of DSBs increased from 33% with spontaneous breakage to 41% with DMSO treatment, followed by a return to 36% with dual drug treatment (Fig. 2D). In contrast, FX cells showed higher level (37%) of DSB-gene association than NM cells in the untreated condition, but remained constant with 36% and 38% in DMSO-treated and dual-treated conditions, respectively (Fig. 2D). These results suggested FX cells are more transcriptionally active than NM cells, whereas NM cells have stronger transcriptional response to drug treatment than do FX cells. Supporting this notion it was shown that FMRP knock-out mouse neurons exhibit increased gene expression compared to control neurons (Korb et al., 2017). We reckoned that the gene-associated DSBs were transcription-related and sought mechanisms for intergenic DSB formation. Delayed replication timing is one of the hallmarks for APH-induced chromosome fragility (Hellman et al., 2000; Le Beau et al., 1998; Palakodeti et al., 2004; Wang et al., 1999). Using published Repli-seq data of the NM cells (Hansen et al., 2010) we divided the genome into 50-kb early- or late-replicating segments and calculated the percentage of DSBs in each segment (Supplemental Information, Supplemental Methods and

Discussion). All six samples showed enrichment of DSBs in late-replicating regions ($p < 10E-3$) (Fig. 2E). Notably, the percentage of DSBs that fall in the early replicating regions is correlated with the percentage of DSBs within genes (Fig. 2F). Together these results suggested two main types of chromosome breakage—those in the intergenic regions that undergo delayed replication and those in the gene-rich early replicating regions that experience elevated level of gene transcription.

Preferential association between drug-induced DSBs and R-loop forming sequences in FX cells. If the gene-associated DSBs were due to drug-induced replication-transcription conflict at actively transcribing genes, DSBs might correlate with R-loop locations. We surveyed a database of R-loop forming sequences (RLFSs) predicted by a previously described algorithm (Wongsurawat et al., 2012) for correlation with DSBs (Supplemental Table S3) . Untreated cells did not show enrichment of spontaneous DSBs at RLFSs; however, DMSO-treated NM and FX cells both showed significant enrichment of DSBs at RLFSs. Notably, DSBs in APH-treated NM cells were no longer enriched at RLFSs whereas those in APH-treated FX cells remained associated with RLFSs. These results were corroborated by the absolute distance measurements between DSBs and RLFSs (Table 1) using GenometriCorr (Favorov et al., 2012). We concluded that 1) DMSO elicits transcriptional response, possibly through oxidative stress (Supplementary Information), in both NM and FX cells and cause DSBs at RLFSs within actively transcribing genes; 2) replication inhibition by APH triggers NM cells to deploy a mechanism to protect genes from DSBs at RLFSs, whereas FX cells lacked such a mechanism. Consistent with our interpretation, APH-specific DSBs in FX cells showed the greatest association with genes compared to DSBs in any other category (Supplemental Table S4). Aggregated distribution of DSBs around RLFSs showed an enrichment of DSBs immediately downstream of the RLFS start as well as immediately upstream of the RLFS end, specifically in the drug-treated FX cells (Fig. 2G&H). Overall, these results led us to conclude that FX cells form DSBs at RLFSs when treated with DMSO, a response that is further enhanced by APH. The correlation between DSBs and RLFSs is the strongest on chromosomes 1, 13, 14, 15, 21, and 22, which contain ribosomal DNA (rDNA) clusters, followed by chromosomes 2, 6, and 12 (Table 1). Notably, the DSBs on the rDNA-bearing chromosomes were not confined to the rDNA loci. We also compared the DSBs to a composite list of DRIP-seq (DNA:RNA hybrid Immunoprecipitation followed by sequencing) signals, generated by merging all DRIP-seq signals in NT2 and K562 cell lines to

minimize cell type-specific differences (Sanz et al., 2016). The results largely recapitulated the comparison between DSBs and RLFSs (Supplemental Table S3). Because RLFS prediction is an unbiased approach, we focused on testing if RLFSs are more susceptible to breakage in FX than in NM cells.

Ectopic expression of FMRP, but not the FMRP-I304N mutant, reduces RLFS-induced DSBs. We employed a modified yeast-based system (Prado and Aguilera, 2005) to measure DSB frequency resulting from programmed transcription-replication conflict induced by human RLFSs, using recombination frequency (RF) as a readout (Fig. 3A). In the absence of RLFS insertion there was a 4.7-fold enhancement of RF on the plasmid with convergent compared to codirectional replication and transcription (Supplemental Fig. S3A), consistent with previous observation (Prado and Aguilera, 2005). Two human RLFSs, when inserted in the sense orientation, each caused elevated RF over the control sequence (non-RLFS), in the convergent replication-transcription configuration specifically (2 and 4 fold, $p=0.0024$ and $p<0.0001$, respectively, Supplemental Fig. S3B). RF was further enhanced in a strain lacking RNase H1, an enzyme known to resolve R-loops by degrading the RNA:DNA hybrid: ~2 and 1.5-fold for sense and anti-sense orientation, respectively, for RLFS-1; and ~1.2 fold for both sense and anti-sense orientations, for RLFS-2 (Supplemental Fig. S3B&C). Because RLFS-2 already induced high RF, further enhancement by eliminating RNaseH1 was only moderate. Next we asked if ectopic expression of FMRP would decrease RLFS-induced DSBs. Expression of empty vector did not alter the RLFS-induced RF (comparing Supplemental Fig. S3B to Supplemental Fig. S3D). A significant drop in RF was observed for expression of FMRP (2 and 1.6 fold for RLFS-1 and RLFS-2, respectively) or a positive control, RNaseH1, but not for a non-specific RNA binding protein She2, compared to empty vector (Fig. 3B). Finally, a mutant FMRP containing an I304N substituion in the KH2 domain, a rare *de novo* mutation that led to FXS (De Boulle et al., 1993; Siomi et al., 1994), no longer suppressed RF (Fig. 3B). We also verified that FMRP and FMRP-I304N showed similar level of protein expression in yeast (Supplemental Fig. S3E). The I304N mutation abolishes FMRP binding to mRNA and the polysome (Feng et al., 1997). Our results thus suggest that the KH2 domain is also involved in interaction with R-loops.

FMRP chromatin binding sites are associated with RLFSs. Our study so far suggests that FMRP binds to its mRNA targets co-transcriptionally and prevents stable R-loop formation. We predicted that some of the previously reported mRNA targets for FMRP are chromatin binding

sites for FMRP. ChIP-seq analysis identified 5238 putative FMRP-binding sites (Fig. 4A). Among them, 54.8% are located in the genic regions, predominantly in the introns (44.7%) (Supplemental Fig. S4A). Select top FMRP-binding genes (*CLNK*, *DLG1*, *ASTN2*, and *ANK1*) were verified with ChIP-qPCR (Supplemental Fig. S4B). At a first pass, surprisingly only 283 FMRP-binding sites in 191 genes overlapped with an RLFS (Fig. 4B). FMRP-binding sites with overlapping RLFSs also showed relatively lower ChIP signals than stand-alone FMRP-binding sites (Supplemental Fig. S4C), indicating genes where these two features overlap are under-represented in the genome ($p < 2.2e-16$, Fisher's exact test). However, the absolute distance between FMRP-binding sites and RLFSs was significantly shorter than expected (Fig. 4C), suggesting that these two entities tend to be adjacent to, rather than overlapping with, each other. Moreover, FMRP-binding sites with overlapping RLFSs are enriched at the promoter and transcription start site (Fig. 4B), a pattern that was not observed for stand-alone FMRP-binding sites. To further demonstrate FMRP is associated with R-loops we examined their co-localization by immunostaining. In untreated cells, co-localization of FMRP and RNA:DNA hybrid was relatively confined to the nuclear periphery and cytoplasm. With drug treatment, the co-localization became enriched in the nucleus (Fig. 5A). Three dimensional volumetric reconstruction further confirmed the co-localization (Supplemental Movie S1). We also asked if FMRP interacts with proteins known to participate in RNA:DNA hybrid resolution. To date we have detected interaction between FMRP and DHX9 (Fig. 5B&C), a helicase that has been shown to suppress R-loop formation and prevents chromosome breakage (Cristini et al., 2018).

Identification of novel FXS-associated genes. We annotated the genes neighboring spontaneous DSBs in NM cells (5 kb maximum distance) and found no significant ($p < 0.001$) GO (Gene Ontology) enrichment. In contrast, spontaneous DSB-associated genes in FX cells were enriched in "neuron projection development", "synapse organization" and "neuron cell-cell adhesion" (Supplemental Table S5). Genes containing overlapping RLFSs and drug-induced DSBs in the FX cells were enriched in polysaccharide metabolism, including flavonoid glucuronidation and membrane organization pathways (Supplemental Table S5). Interestingly, 3993 genes associated with the 5238 FMRP-binding sites were also enriched in flavonoid/xenobiotics metabolism ($p = 0$; Fig. 4D). The end step of phase II xenobiotics metabolism is glucuronidation catalyzed by the uridine diphosphoglucuronosyl transferases (UGTs) comprised of the UGT1 and UGT2 families. The UGT1 family is derived from a single

gene locus through alternative splicing and joining of an isoform-specific exon 1 with four common exons 2-5 (Fig. 4E). The *UGT1* family, and not *UGT2*, contain co-localized FMRP-binding sites and FX-specific DSBs, the latter of which can potentially impact the expression of all isoforms by virtue of residing in the intron preceding the common exons 2-5 (Fig. 4F). Only *UGT1A1* is possibly spared as the DSBs precede exon 1 sequence for *UGT1A1*. Two phase I xenobiotics metabolic genes, *CYP2C9* and *CYP2C19*, also contain FX-specific and drug-induced DSBs (Supplemental Fig. S5A&B). We report that untreated FX cells showed ~2 fold reduction of UGT1 expression compared to NM cells, and greater reduction was seen in drug-treated FX cells (Fig. 4G). Similarly, FX cells showed reduction of CYP2C9 expression (Fig. S5C). We also honed in on 487 genes harboring overlapping or adjacent (< 1 kb apart) FMRP binding sites and RLFSs (Supplemental Table S7), which we considered as "at risk" genes for FXS even though proximal DSB was not observed. Expression of these genes was enriched in the brain ($p = 5.7E-2$) and particularly, in amygdala ($p = 3.0E-2$). There was also a moderate enirchment of genes in "learning or memory" ($p = 6.7E-1$, Supplemental Fig. S4D). Finally, 16 of 36 previously validated mRNA substrates for FMRP (Sethna et al., 2014) were identified as its chromatin-binding sites and/or APH-induced DSBs in FX cells, with 4 genes (*GRIA1, GRM5, MTOR,* and *PTEN*) containing both (Supplemental Fig. S4E), highlighting the roles of glutamate receptors and mTOR signaling in FXS.

The FX lymphocytes-associated phenotypes are recapitulated in FX fibroblasts. So far all our experiment had been done with lymphoblastoid cell lines. To ensure that the observed FX-associated phenotypes were not due to a tissue-specific artifact, we performed select experiments with fibroblasts derived from a FX individual, GM05848, which contains a full mutation of 700 CGG repeats at *FMR1* (Sheridan et al., 2011) and from a sex- and age-matched unaffected control (GM00357). We confirmed that FX fibroblasts also showed increased DNA damage by γH2A.X staining, particularly during drug treatment (Fig. S6A&B). This was accompanied by the observation that FX fibroblasts also showed increased RNA:DNA foci formation in the nucleus upon drug treatment (Fig. S6C), consistent with increased R-loop formation in these cells. Moreover, the fibroblast cells—with their larger nuclei—enabled the detection of RNA:DNA foci localizing to what appeared to be dark areas of the nucleus, possibly the nucleoli (Fig. S6C).

DISCUSSION

FMRP as an R-loop regulator and a guardian of genome integrity. The main discovery from our study is the genome-wide chromosomal breakage in FX cells, with or without replication stress, suggesting FMRP is a guardian of the genome. This represents a novel development in our understanding of the FXS etiology. FX cells were defined by the detection of a fragile site named FRAXA at the *FMR1* locus, specifically induced by folate stress, in individuals with full mutation of the CGG repeat expansion. While there were an abundance of studies measuring FRAXA site expression, relatively few compared the number of common fragile sites (CFSs), which are induced by APH, in FX cells to controls. One study reported more than 3 fold increase of the rates of CFSs in FX patients (27.9%) compared to unaffected controls (7.9%) when treated with APH (Murano et al., 1989). However, the authors did not emphasize this difference and concluded that age difference between the test and control groups may have confounded the results. We surmise that this was an unexpected finding which led to the down-played conclusion. We also note that these earlier studies were based on a cytological screening method with low resolution and sensitivity, guided by primary focus on detecting FRAXA in the FX cells. Thus, it is owing to the Break-seq technology with its unparalleled sensitivity that the detection of global DSB formation in the FX genome was enabled, a testament to the utility of Break-seq in other disorders with underlying etiological basis of genome instability. We note that the global induction of DSBs in the FX genome was first detected as increased γH2A.X stainining in FX cells. This observation apparently differs from a previous study reporting decreased γH2A.X staining in embryonic fibroblasts from an *FMR1* knock-out mouse model (Alpatov et al., 2014). As the mutation in the FX individual is repeat expansion-induced epigenetic silencing of *FMR1*, whereas the mutation in the mouse model involves the deletion of exon 5 of *FMR1*, we suggest that the apparent discrepancy in our observations stemmed from these key differences in our experimental systems.

A related key discovery is the correlation between drug-induced DSBs and RLFSs in FX cells, prompting the hypothesis that FMRP is an R-loop processor, and therefore a transcription regulator, which places it functionally upstream of mRNA transport and translation. This new function of FMRP is supported by the suppression of RLFS-induced recombination during programmed replication-transcription conflict by FMRP, dependent on its KH2 RNA-binding

domain. It is further strengthened by FMRP binding to chromatin sites adjacent to RLFS, which in turn associates with DSBs. It is also consistent with the known affinity of FMRP for, in descending order of degree, RNA, ssDNA and dsDNA (Ashley et al., 1993), three substrates are simultaneously present in an R-loop. Lastly, lending further support to our hypothesis we detected interaction between FMRP and DHX9, a known R-loop regulator. Furthermore, FMRP was reported to interact with the THO/TREX complex, a mRNP transporter known to be important for R-loop prevention (Dominguez-Sanchez et al., 2011), through affinity purification (Hein et al., 2015). This new function of FMRP has profound implications for FXS etiology as it adds another layer of complexity to the impact of FMRP deficiency. It also suggests a potential therapeutic intervention by targeting co-transcriptional DNA:RNA hybrids in FX cells.

A potential mechanism linking dysregulated protein synthesis to genome instability in FX cells. FMRP is predominantly localized to the nuclear periphery and in the cytoplasm in the absence of DNA damage. Replication stress induces co-localization of FMRP and RNA:DNA hybrids towards the center of the nucleus in the lymphoblastoids. Fibroblast nuclei staining further suggests RNA:DNA hybrids localizing to the nucleous in FX cells. These results are consistent with the observed correlation between DSBs and RLFSs, preferentially occurring on rDNA-bearing chromosomes, which are resident of the nucleolus. Do DSBs have affinity for the nucleolus as a locale, or is there an underlying cause for the rDNA-bearing chromosomes to generate RLFS-associated DSBs? We favor the latter explanation. While the 45S rDNA array residing on the short arms of five acrocentric chromosomes (13, 14, 15, 21, and 22) defines the nucleolus, the 5S rDNA array is a resident of chromosome 1 and the 5S and 45S rDNA arrays are not in close proximity spatially in human lymphoblastoid cells (Yu and Lemos, 2016). This suggests that DSB-RLFS association on these chromosomes is not mediated by proximity to the nucleolus *per se*. Instead we reason that the act of rRNA transcription subjects these chromosomes to increased R-loop formation and chromosome breakage, outside the rDNA arrays. FMRP deficiency leads to elevated level of protein translation (Darnell et al., 2011), which would be reliant on increased rate of ribosome production. Conceivably, FX cells must sustain high level production of ribosome and therefore, rRNA transcription, and thus relay the stress from the rDNA loci intra-chromosomally onto the remainder of the chromosome. Torsional stress of the chromosome, when combined with replication stress, may induce heightened replication-transcription conflicts and chromosome breakage.

Novel cellular pathways linked to FXS through genome instability. Neuronal development genes appeared susceptible to strand breakage in FX cells even without drug treatment. Additionally, genes containing overlapping RLFSs and drug-induced DSBs in FX cells are enriched in flavonoid glucuronidation. Moreover, genes containing FMRP-binding sites are also enriched in flavonoid metabolism. These results led us to hypothesize that FX cells, when under stress, are defective in glucuronidation of xenobiotics. Glucuronidated flavonoids have a reported protective role towards a range of neurological disorders (Docampo et al., 2017). Conversely, decreased glucuronidation of xenobiotics such as bisphenol A has been observed in patients with Parkinson's Disease (Landolfi et al., 2017). Finally, metabolic profiling of *FMR1* premutation carriers who have intermediate (55-200 copies) CGG repeat expansion but nevertheless manifest FMRP deficiency, showed elevated levels of glucuronic acid (Giulivi et al., 2016). We found FX-specific DSBs in genes coding for the most important enzymes in phase I (cytochrome P450 enzymes, specifically CYP2C9 and CYP2C19) and phase II (UGTs, specifically the UGT1A subfamily isoforms) xenobiotics metabolic pathways. We further demonstrated that both UGT1 and CYP2C9 expression levels are reduced in FX cells. The UGT1A subfamily enzymes glucuronidate bilirubin, xenobiotic phenols, and a wide range of psychotropic drugs (de Leon, 2003). Bilirubin glucuronidation is catalyzed by UGT1A1, the single enzyme that may be spared by DSB formation at the *UGT1* locus. Consistently, we have not come across any report of hyperbilirubinemia in FXS patients. Therefore we suggest that FX individuals are defective in metabolizing xenobiotics and psychotropic drugs, which can lead to neurotoxicity and further perils of the neurological functions.

In summary, our study led us to present a model (Fig. 6) where FMRP associates with its mRNA substrates co-transcriptionally. Upon replication stress and drug-induced gene expression, FMRP increases its nuclear presence to prevent R-loop formation and chromosome breakage during heightened replication-transcription conflicts. We note that FX cells also produce spontaneous DSBs at a higher level than NM cells, and these spontaneous DSBs are not correlated with RLFSs. This suggests that FMRP has additional protective role(s) towards the genome without external replication stress. Recent studies have shown that FMRP deficiency causes imbalance of epigenetic modifications due to unregulated protein synthesis (Korb et al., 2017; Li et al., 2018). It is plausible that the spontaneous chromosome breakage in FX cells is a result of altered histone modifications predisposing specific regions of the chromatin to

breakage. Together with our discovery that FMRP directly interacts with the chromatin, these attributes make FMRP a novel mediator of transcription and replication whose function is to prevent R-loop accumulation and ensure genome integrity, thereby maintaining normal synaptic plasticity in neuronal cells. Finally, our study marks a technological advance in mapping chromosome breaks by Break-seq, previously developed for the model organism *Saccharomyces cerevisiae* (Hoffman et al., 2015). To this date, Break-seq has shown efficacy in multiple mammalian cell systems including suspension cell culture (this study), adherent cell culture and 3D organoids (unpublished). Thus, we believe Break-seq holds tremendous potential as a powerful tool for genome discoveries.

ACKNOWLEDGEMENTS

We wish to thank V. Van Steenkist for systems and programming support; Drs. C. Dobkin, B. Howell and A. Aguilera for generous gift of antibodies and plasmids; and Drs. X. Chen, L. Kotula, F. Middleton, and T. Wongsurawat for helpful discussions. We also thank the staff at SUNY Upstate Flow Cytometry Core and the University at Buffalo Genomics Core for flow sorting and HiSeq sequencing, respectively. This work was supported by the NIH awards (5R00GM08137805 and 5R01GM11879901) and the Department of Defense CDMRP Discovery award (PR141850) to W.F. and institutional support from A*STAR and SUNY EMPIRE scholar grant to V.A.K.

AUTHOR CONTRIBUTIONS

A.C., A.M., B.H., E.H., and W.F. conceived the study and designed the experiments. A.C., A.M., E.H., A.B. and W.F. performed the Break-seq experiments. A.C. and B.H. performed the ChIP-seq experiments. A.C., J.L., and H.H. performed and analyzed the immuno-staining experiments. A.C. and A.T. performed the recombination assays. A.C. performed and analyzed the flow cytometry, chromatin fractionation, and ChIP-qPCR studies. P.J., V.K., S.E.H., C.C. and W.F. performed computational analyses. A.C. and W.F. wrote the manuscript with input from all authors;

DECLARATION OF INTERESTS

The authors declare no competing interests.

FIGURE LEGENDS

Figure 1. **Fragile X cells show elevated DNA damage in vivo.** (**A**) Flow cytometry analysis shows that APH treatment enriches for cells in S phase. Three independent experiments were performed and one representative experiment is shown. (**B**) Flow cytometric sorting of γH2A.X-positive cells under APH-induced replication stress. Bars indicate mean and standard deviation for three independent experiments (except for 0.6 μM APH for which two experiments were performed). Two-way ANOVA test p values: *p<0.05, ***p<0.001, ****p<0.0001. Ten thousand cells were analyzed in each flow experiment. (**C**) Single cell view of γH2A.X foci distribution, expressed as mean integrated density (FIRE, LUT) for the indicated samples, in NM and FX cells. (**D**) 3D surface plots of γH2A.X intensity distribution in the cells from **(C**), x and y axes are in microns and the z axis is expressed as pixel intensity after thresholding at each focus (FIRE, LUT), in NM and FX cells.

Figure 2. Break-seq mapping shows high level of DSBs in FX cells and drug-induced DSBs in FX correlate with RLFSs. (A) Break-seq methodology. (**B**) Chromosomal distribution of the number of DSBs per Mb of DNA in the indicated categories. **(C)** Venn diagrams showing the concordance between samples of different treatments. FX cells show "reprogramming" of drug-induced DSBs compared to those in the untreated cells. **(D)** Distribution of DSB peaks relative to genes in the indicated samples. Genic features include introns, exons, 5'- and 3'-UTRs, promoters, and the immediately downstream (<1 kb from the 3'-UTR) regions (ImmediateDownstream). (**E**) Distribution of DSBs in early vs. late replicating regions of the genome, as defined by Hansen RS et al, in the indicated samples. See Methods for details. (**F**) Correlation between the percentage of DSBs associated with genes and the percentage of DSBs with early replication timing. Aggregated DSBs from the indicated samples around the start **(G)** or the end **(H)** of R loop forming sites (RLFSs) in a 4000 bp window centering on the RLFS.

Figure 3. **FMRP expression suppresses RLFS-induced DSB formation.** (**A**) A non-functional *LEU2* marker containing two inserted direct repeats and driven by a galactose-inducible *GAL1* promoter was placed next to an origin of replication (*ARSH4*) such that the

direction of transcription is convergent or codirectional with respect to the direction of the proximal replication fork. Upon galactose induction, convergent replication and transcription would induce DSBs and homologous recombination repair to generate a functional *LEU2*, resulting in leucine prototrophy. Two RLFSs from the human genome (RLFS1-1 from the promoter of *FMR1* and RLFS-2 from intron 5 of Fragile Histidine Triad) were inserted between the direct repeats to test for enhanced DSB and recombination. A non-RLFS sequence without predicted R-loop forming propensity and with similar G-richness in both strands served as control. All sequences were similar in size (~500 bp). The RLFSs were inserted in the sense or anti-sense orientation with respect to *LEU2* transcription (*i.e.*, G-rich strand on the non-template or template strand, respectively), with the sense orientation expected to preferentially induce R-loop formation. The control sequence was also inserted in two orientations and no difference in RF was observed between them (Fig. S3C). RF is calculated based on the percentage of leucine prototrophs after plating. (**B**) The effect of ectopic expression of indicated genes on the pRS313 plasmid, under the CMV promoter, on RLFS-induced RF. Bars indicate mean and standard deviation between biological replicates (n=3). P values for Two-way ANOVA test: *, $p<0.05$; ***, $p<0.001$; ****, $p<0.0001$. See Figure S3 for additional control experiments.

Figure 4. Analysis of chromatin binding sites of FMRP. (**A**) Distribution of the number of FMRP binding sites (FBSs) per chromosome. (**B**) Distribution of the FBSs inside genic regions, and in regions upstream of TSS (Transcription Start Sites) and TES (Transcription End Sites). Red, green and blue lines represent distribution of 5238 FBSs, 283 FBSs with overlapping RLFS and 4955 FBSs without overlapping RLFS, respectively. (**C**) Observed absolute distance between FBSs and RLFSs (blue) compared to the expected distance if uncorrelated (black line). (**D**) Biological processes derived from WebGestalt (WEB-based GEne SeT AnaLysis Toolkit) that are enriched for those genes bound by FMRP; FDR, false discovery rates. (**E**) Schematic representation of UGT1A subfamily alternative splicing isoforms. (**F**) UCSC genome browser screen shot of FX-specific DSBs shown as vertical bars (upstream of the gene, cyan box; in the intron preceding the common exons 2-5, orange boxes) in *UGT1* family genes. (**G**) Representative Western blots of UGT1 protein expression with GAPDH as control and

quantification using ratio of UGT1 to GAPDH derived from three biological replicates. Error bars denote standard deviation. P values that are < 0.05 from Two-way ANOVA test are shown.

Figure 5. FMRP is co-localized to R-loop forming sites and co-immunoprecipitates with DHX9. (**A**) Co-localization of FMRP and RNA:DNA hybrids. Immunofluorescence images of untreated, DMSO- and APH-treated NM cells co-stained for RNA:DNA hybrids (cyan), FMRP (magenta) and nucleus (yellow, outlined). Immuno-staining is shown in a single Z-plane. Scale bar, 5 μm. (**B**) Co-immunoprecipitation of FMRP and DHX9 using the anti-FMRP monoclonal antibody (Covance) to pull down FMRP and immunoblotted for both FMRP and DHX9. GAPDH served as negative control. The asterisks indicate the lower band of a doublet signal in the "IP-FMRP" lanes is the DHX9 protein, which is present in the FMRP-immunoprecipitated complex and absent in the IgG-precipitated control complex ("IP-IgG" lanes). Substantial fraction of DHX9 is also present in the first wash (Wash 1) of the immunoprecipitate, likely due to the abundance of DHX9. LE, long exposure; SE, short exposure. (**C**) Reciprocal immunoprecipitation using anti-DHX9 and blotted for both DHX9 and FMRP, with GAPDH serving as negative control.

Figure 6. Proposed model of a novel FMRP function in the nucleus. (A) Illustration of a normal lymphoblastoid cell without any treatment, showing FMRP in the cytoplasm and in the nuclear periphery possibly engaged in mRNA transport. **(B)** Under replication stress, FMRP localizes to the center of the nucleus at R-loop formation sites in genes induced by DMSO and APH. At the junction of convergent replication and transcription, FMRP in conjunction with DHX9 and possibly the THO/TREX complex is involved in R-loop removal and avoidance of a deleterious collision (inset). dsDNA, double-stranded DNA. **(C)** In FX cells increased protein synthesis rate demands high level rRNA production on the rDNA-bearing chromosomes, which in turn causes increased level of (RNA Pol II) transcription elsewhere on these chromosomes, represented by the chromosome loops tethered to the nuclear pores for active transcription. Absence of FMRP permits stable R-loop formation and DSBs upon collision of replication and transcription (inset). The involvement of DHX9 and the THO/TREX complex in this context remains to be determined. ssDNA, single-stranded DNA.

TABLES

Table 1. Statistical analysis of absolute distance between RLFSs and DSBs in the indicated categories on each chromosome using GenometriCorr. Shown are the projection test p-values (P) and projection test observed to expected ratios (R). Samples with R values greater than 3.5 are shown in red.

Chr	FX.Untreated		FX.DMSO		FX.APH		NM.Untreated		NM.DMSO		NM.APH	
	P	R	P	R	P	R	P	R	P	R	P	R
1	0.355	1.041	**2.22e-16**	**3.799**	1.07e-14	2.764	0.224	1.239	0.086	1.514	0.353	0.816
2	0.314	0.644	**2.21e-11**	**3.625**	1.55e-10	2.629	0.236	1.212	**1.73e-06**	**3.797**	0.010	1.850
3	0.446	0.691	1.29e-06	3.028	1.81e-07	2.579	0.329	0.000	0.024	2.283	0.131	1.430
4	0.283	0.398	2.39e-05	3.008	1.44e-10	3.227	0.355	0.801	0.036	2.209	0.199	1.281
5	0.217	0.348	1.09e-06	3.244	1.63e-08	2.799	0.244	0.000	0.007	2.553	0.148	1.382
6	0.090	0.000	**6.36e-07**	**3.746**	5.08e-04	2.065	0.336	0.000	0.134	1.533	0.028	0.000
7	0.489	0.868	6.30e-06	2.515	4.01e-10	2.575	0.108	0.000	0.104	1.483	0.126	1.339
8	0.150	0.298	4.34e-06	2.965	1.06e-04	2.085	0.182	1.362	0.203	1.294	0.131	0.407
9	0.301	0.413	3.91e-07	3.217	4.19e-12	3.197	0.174	1.392	0.016	2.174	0.109	0.461
10	0.137	0.289	2.85e-07	3.279	3.85e-09	2.806	0.302	1.041	0.088	1.638	0.373	1.012
11	0.070	0.233	7.45e-05	2.213	0.001	1.643	0.118	0.000	0.047	1.708	0.123	0.528
12	0.044	0.000	**4.91e-11**	**4.040**	7.32e-09	2.743	0.209	0.000	0.076	1.703	0.350	1.040
13	0.372	0.000	**9.55e-08**	**6.960**	**8.71e-10**	**5.431**	0.347	0.000	0.482	0.000	0.260	0.000
14	0.190	1.333	**8.41e-06**	**3.516**	**6.05e-11**	**3.813**	0.035	2.782	**5.87e-04**	**4.219**	0.103	1.620
15	0.109	1.655	**3.62e-07**	**4.231**	**2.64e-11**	**3.926**	0.377	0.000	0.054	1.962	0.088	1.636
16	0.050	0.214	**0.00e-00**	**5.667**	**0.00e-00**	**4.522**	0.484	0.769	0.060	1.626	0.291	1.112
17	0.056	0.221	2.62e-08	3.289	7.21e-13	3.158	0.322	0.434	0.353	1.048	0.165	1.273
18	0.103	1.786	**1.14e-04**	**3.962**	3.54e-04	2.763	0.144	1.498	0.061	2.238	0.237	1.191
19	0.057	0.459	2.32e-04	1.941	2.88e-07	1.916	0.162	0.446	0.429	0.999	0.065	0.635
20	0.456	0.803	5.62e-04	2.831	9.08e-08	3.164	0.135	1.568	0.039	2.140	0.218	1.239
21	0.230	0.000	**5.01e-09**	**7.108**	**2.22e-13**	**6.001**	0.426	0.000	0.014	2.812	0.432	0.895
22	0.093	0.000	**1.80e-09**	**5.343**	**3.99e-10**	**3.764**	0.462	0.646	0.016	2.142	0.009	2.158
X	0.184	1.351	0.081	1.482	0.098	1.339	0.113	1.636	0.024	2.132	0.077	1.555
ALL	5.47e-06	0.528	0	3.162	0	2.684	0.041	0.715	8.93e-14	1.976	0.150	1.088

MATERIALS AND METHODS

Cell line growth and drug treatment conditions. Human EBV transformed lymphocyte cell lines, GM06990 (control) and GM03200 (Fragile X), and fibroblast cell lines, GM00357 (control) and GM05848 (Fragile X), were purchased from Corielle institute. Lymphoblastoids were grown in RPMI1640 (Corning cell gro), supplemented with GlutaMAX (GIBCO), 15% heat-inactivated FBS (Fetal Bovine Serum, Benchmark), 100 IU/mL penicillin and 100 µg/mL streptomycin (Corning cell gro) at 37°C with 5% CO_2. Fibroblast cells were cultured in MEM culture media with 15% FBS (Corning), 1X GlutaMAX, 100 IU/mL penicillin and 100 µg/mL streptomycin. Lymphoblastoid cells were treated, at a density of 0.4-0.5x10^6 cells/ml, with 0.03 µM, 0.3 µM, or 0.6 µM APH (A. G. Scientific), solvent (DMSO, 0.02%, same as the concentration in the APH-treated samples) only, or nothing, for 24 h before harvest. Fibroblasts were treated at 30-40% confluency with the same drug concentrations.

Flow cytometry for cell cycle analysis. Approximately 1.5-2x10^6 cells from the Break-seq experiments were harvested for flow cytometry. Cells suspended in 1 ml of PBS were slowly added to chilled absolute ethanol and stored in -20ºC. Fixed cells were pelleted at 250xg for 15 m at room temperature and then rehydrated with 5 ml PBS for 15 m. Cells were again pelleted and resuspended at 0.5x10^6 cells/ml in propidium iodide solution (40 µg/ml propidium iodide, 100 µg/ml RNase A in PBS) and incubated for 20 m at 37ºC. Cells were passed through filter-topped flow tubes (BD Falcon) using a luer-lock syringe and analyzed using Becton Dickinson Fortessa Cell Analyser (BD Biosciences). Data were analyzed by FlowJo.

Flow cytometry for quantification of cells stained for γH2A.X. Approximately 3x10^6 cells were treated with APH, DMSO or nothing. For compensation control, an additional 3x10^6 cells were subjected to 2 flashes of UV irradiation at 20 µJ/cm^2 and allowed to recover for 4 h before harvest. Cells were treated with 1:500 diluted Zombie Aqua (Violet, Biolegend) to stain dead cells, followed by a wash in FACS buffer (2% FBS in PBS). Cells were then fixed in 500 µl of 4% paraformaldehyde, permeabilized by 500 µl methanol, and stained with 100 µl of a 1:50 dilution of anti-γH2A.X in dilution buffer (0.5% BSA in 1x PBS) for 1 h. Cells were then centrifuged and washed in dilution buffer followed by 1x PBS. Cells were resuspended in FACS buffer and filtered through filter-topped flow tubes (BD falcon) using a luer-lock syringe.

Samples were analyzed using Becton Dickinson Fortessa Cell Analyser (BD Biosciences) and data analyzed by FlowJo. Dead cells were removed from the analysis. Stained but untreated NM cells were used to generate a baseline for fluorescence. Cells with DNA damage were gated based on fluorescence intensities (FI) higher than the baseline. Percentage of cells with DNA damage were calculated based on the number of cells above the baseline FI and total live cells.

Immunocytochemistry and microscopy. *For lymphoblastoids:* Approximately $3x10^6$ cells having undergone drug treatment described above were washed twice in PBS before fixing with 500 µl of methanol or 4% paraformaldehyde in microfuge tubes. *For firbroblasts:* Approximately $1x10^5$ cells were plated on poly-D-lysine (Sigma Aldrich)-coated coverslips and cultured for 72 h, followed by drug treatment for 24 h. *For both lymphoblastoids and fibroblasts:* Cells were washed with 500 µl 1X PBS twice, fixed with 500 µl 4% paraformaldehyde for 20 m at room temperature, followed by gently washing with 1X PBS three times. Cells were then blocked with 500 µl PBSAT (1% BSA, 0.5% Triton X in 1X PBS), followed by incubation with 100 µl of primary antibody solution for 1 h, washed with PBSAT, and incubation with 100 µl secondary antibody for 1 h. Cells were then washed with PBSAT followed by PBS, and resuspended in mounting media (Prolong Diamond antifade plus DAPI, Invitrogen) before being placed as a drop onto microscope slides. Coverslips were carefully placed on top of the mounted drops and allowed to solidify for 24 h before imaging on Leica STP 800 wide-field fluorescence microscope (for lymphoblastoids) or Leica SP8 confocal (for fibroblasts). Antibodies used for immunostaining include the following: primary antibodies (anti-γH2A.X, Cell Signaling, 1:500; anti-FMRP, Cell signaling, 1:200; S9.6, Kerafast, 1:500 for lymphoblastoids and 1:120 for fibroblasts; and anti-Lamin A&C, Novus Biologicals, 1:250) and secondary antibodies (Alex fluor 488, 568, and 647, Invitrogen, 1:400).

To quantify γH2A.X staining signals maximum projection of 3D image stacks acquired from thirty-six 2D imaging planes with a step size of 0.2 micron along the z-axis was performed using the MetaMorph software (Molecular Devices). Image stacks were deconvolved using the AutoQuant software. In Fiji, DAPI was used to create region of interest (ROI) of nuclei in γH2A.X channel for individual cells. Maximum intensity projections adjusted for background in Fiji were used to quantify γH2A.X intensities in ROI for approximately 28-35 cells. Representative images adjusted for background and contrast are shown. FIRE LUT was used to

show intensities of foci per nuclei in every sample. 3D surface plots were also conducted in Fiji (plot parameters: filled, 0.2 perspective, FIRE LUT, 0.88 scale, 0.87 z-scale, 100% max and 19% min) as a measure of the intensities of foci per nuclei per sample. Statistical analysis was done using GraphPad Prism 7 and values were plotted in Kaleidagraph.

To determine co-localization of FMRP and R-loop in the nucleus, 3D image stacks were acquired from sixty-one 2D imaging planes with a step size of 0.11 micron using Metamorph. For images shown in Fig. 5 a single Z-plane image at approximately the center of the stack was shown for each sample. DAPI was used to create a ROI which was overlayed and colored white to indicate nucleus in all three channels (DAPI, FMRP, S9.6). Images were adjusted for background and contrast and smoothed using a gaussian blur of 0.7 in Fiji. 3D construction of the image stacks were performed in Metamorph with rotation along the X-axis every 10° for FMRP and S9.6 channels, followed by conversion into a movie using Metamorph.

Break-seq and ChIP-seq. Lymphoblastoids GM03200 and GM06990 were used for Break-seq and ChIP-seq analyses. For Break-seq three independent sets of experiments were performed, wherein Set A and B were technical replicates from the same experiment and Set D and E were biological replicates. Break-seq library construction was performed as previously described (Hoffman et al., 2015) with modifications. For ChIP-seq to identify FMRP chromatin binding sites one experiment was performed, followed by independent validation of target genes by ChIP-qPCR. Detailed procedures are described in the Supplemental Information.

Calculation of replication timing for DSB regions. Replication timing data were derived from Repli-seq data of lymphoblastoid GM06990 cells (accession: ENCSR595CLF) publicly available from ENCODE (https://www.encodeproject.org/replication-timing-series/ENCSR595CLF/). An S50 ($0<S50<1$) value, defined as the fraction of the S phase at which 50% of the DNA is replicated (50% of the cumulative enrichment), was computed for any 50-kb segment of the genome (Hansen et al., 2010). The cumulative enrichment was calculated for each sliding window of 50 kb at a 1-kb step size by linear interpolation of enrichment values in 6 evenly divided temporal windows of the S phase, as previously described (Chen et al., 2010). If a given 50-kb segment was not significantly enriched in any window in the S phase, no S50 value was attributed (S50=NA). Approximately 5% of the genome fell in this category. The DSB regions were then assigned the same S50 values as that of the 50-kb segment in which they reside. For

FX cells DSBs on the Y chromosome were excluded from further analysis due to the lack of replication timing data in the reference genome of GM06990. Finally, the DSBs with assigned replication timing values were further parsed into early (S50<0.5) and late (S50>0.5) replicating domains. The resulting distribution of DSBs in the early and late replicating domains was subjected to a Genomic Association Test (GAT) to determine if the DSBs were enriched in either of the two domains through 1000 randomized simulation (Heger et al., 2013).

Co-immunoprecipitation (Co-IP). Approximately 6-7 x10^6 cells were used for each IP reaction. Cells were resuspended in 1 ml IP lysis buffer [25 mM Tris-HCl pH 7.5 / 150 mM NaCl / 1% NP-40 / 1 mM EDTA / 5% glycerol / Halt protease inhibitor cocktail (Thermo scientific) / Halt phosphatase inhibitor cocktail (Thermo scientific)] and incubated on ice for 1 h. Cell lysates were centrifuged at 10,000 rpm for 10 min. Protein concentration in the supernatant was determined using Pierce protein assay reagent (Thermo Scientific). 50 µl of Dynabeads protein G (Invitrogen) per reaction were incubated with 200 µl antibody binding buffer [1X PBS/ 0.02% Tween 20] and 5 µg of anti-FMRP (Covance), or anti-DHX9 (Santa Cruz Biotechnology), or IgG (Biolegend) in a rotator for 10 m at room temperature. The immuno-complex was rinsed with 200 µl antibody binding buffer at room temperature, followed by incubation with 500 µg of cell lysate per reaction at 4ºC overnight. After incubation the supernatant was saved as flow-through (FT) and the beads were washed twice with IP lysis buffer without NP-40, saving each wash. 50 µl 2X Laemmli buffer was added to the beads and boiled for elution, before analysis on 8% SDS-PAGE gels and western blotting using anti-FMRP (Cell signaling, 1:500), anti-GAPDH (Thermo scientific, 1:4000) or anti-DHX9 (Santa Cruz Biotechnology, 1:500).

Yeast strains and plasmids. Yeast strains used in this study were BY4741 (*MATa his3Δ1 leu2Δ0 ura3Δ0 met15Δ*) and its isogenic derivative *rnh1Δ* (*MATa ura3Δ0 leu2Δ0 his3Δ1 met15Δ0 rnh1Δ::KAN*, EUROSCARF collection (Entian et al., 1999)). Yeast cells were either grown in YEPD or synthetic complete (SC) media with specific amino acids omitted as indicated. All yeast strains were grown at 30ºC with horizontal shaking for liquid cultures. Yeast centromeric plasmids pARS-GLB-OUT (OUT) and pARS-GLB-IN (IN) containing GAL-OUT/IN recombination constructs were provided by and described previously (Prado and Aguilera, 2005). Specifically these plasmids were designed with the *leu2Δ3*'::*leu2Δ5*' direct-repeat recombination system under the *GAL1* promoter. The plasmid also contains *ARSH4,*

URA3, CEN6 and the 83 bp $(C\text{-}A1\text{-}3)_n$ telomeric sequences from pRS304 lacking the *Eco*RI site at the polylinker. Human gene sequences for recombination assay (see below) were cloned between the direct-repeat recombination system (*leu2Δ3':sequence: leu2Δ5'*) using *Bgl*II. The following primers containing *Bgl*II site in the forward and *BamH*I site in the reverse were used for the described sequences: a) control-1_**F**-5'-TCagatctTCAGGCTGCACATTCTTTTC-3' and control-1_**R**-5'-CTCggatccTGCTTTCACTGCAGTTCC-3'; b) control-2_**F**-5'-CTCagatctTGATAATTACAAGGTACACGTTATTGC-3' and control-2_**R**-5'-CTCggatccTTGGTTAGGATAATAAGCACTATGG-3'; c) RLFS-1_**F**-5'-CTCagatctGTAGACGCCTCACCTTCTGC-3' and RLFS-1_**R**-5'-CTCggatccTGCGGGTGTAAACACTGAAA-3'; d) RLFS-2_**F**-5'-CTCagatctCATAACTAAGCACTGTATGCC-3' and RLFS-2_**R**-5'-CTCggatccCCTAGGGACAAGGGGAGGTA-3'

The above sequences were PCR amplified from human genomic DNA (http://www.fenglab-genomestabilityresearch.org/p/isolation-of-genomic-dna-from-mammalian.html). Sequences were inserted in two orientations due to compatibility of ends generated by *Bgl*II and *BamH*I and both the orientations were used to measure recombination frequencies for all sequences. The sequences were inserted in both the IN and the OUT constructs. pFRT-TODestFLAGHAhFMRPiso1 plasmid (Addgene) was used to subclone an *Spe*I/*Bcl*I-digested CMV-FMRPiso1 fragment into pRS316 at the *Xba*I and *BamH*I cloning sites. The resulting construct, pRS316-CMV-FMRPiso1, was then digested with *Not*I and *Eco*RI to obtain the CMV-FMRPiso1 fragment. The fragment was subcloned into pRS313 digested with *Not*I and *Eco*RI producing the final construct pRS313-CMV-FMRPiso1. pRS313-CMV-FMRPiso1I304N was generated using the same procedure from the pFRT-TODestFLAGHAhFMRPiso1I304N plasmid (Addgene).

Recombination frequency assay. The IN and OUT plasmids were first transformed in BY4741 or *rnh1Δ* and selected in SC without uracil in 2% glucose. The fluctuation assay was performed as previously described with modifications (Prado and Aguilera, 2005). Briefly, selected transformants were streaked onto SC-URA+2% Glucose and SC-URA+3% Galactose. Plates were incubated for 4 days at 30ºC to suppress or induce transcription through the *GAL1* promoter respectively. Six single colonies for every sample were re-suspended in 1 ml –N media (1.61 g/l YNB without $(NH4)_2SO_4$ or amino acids, 94 mM succinic acid and 167 mM NaOH) and

sonicated. Serial dilutions were prepared for each of the six colonies per sample: 1:15, 1:150 and 1:1500 in a 96-well plate. 100 µl of diluted samples were plated in SC-URA+3% Galactose for calculation of totals. For calculation of recombinants; 100 µl from undiluted was plated onto SC-LEU-URA+3% Galactose. Plates were incubated for 3 days at 30ºC, and colonies were counted to calculate recombination frequency as follows:

*no. of recombined colonies/(total no. of cells plated*dilution factor)*10^4*

Recombination frequency was calculated for each of the six colonies per sample and the median value was used as the recombination frequency of a sample. Three independent experiments were conducted for each construct and treatment (glucose and galactose) and standard deviations were calculated for graphical representation and to estimate error.

For experiments with FMRP expression the IN and OUT plasmids with or without RLFS were co-transformed with pRS313-CMV-FMRPiso1, pRS313-CMV-FMRPiso1I304N or pRS313 into BY4741 and selected in SC-URA-HIS+2% glucose. Recombination frequency assay was conducted as described above with the totals plated in SC-URA-HIS+3% galactose and the recombinants were plated in SC-LEU-URA-HIS+3% galactose.

Western blot. For UGT1 expression in lymphoblastoids, whole cell lysates were analyzed by 10% SDS-PAGE. The following antibodies were used: anti-FMRP (Covance, 1:1000), anti-UGT1A (Santa Cruz Biotechnology, 1:250), anti-CYP2C9 (Invitrogen, 1:1000) and anti-GAPDH (Thermo scientific, 1:2000). For yeast whole cell extracts, a single colony was inoculated in 10 ml SC-HIS-URA and grown overnight. Cells were centrifuged at 3000 rpm for 5 m, frozen and stored at -80˚C until further use. Frozen cell pellets were thawed in 250 µl TBS [50 mM Tris pH 7.5 / 100 mM NaCl / Halt protease inhibitor cocktail (Thermo scientific)]. Cell suspension was vortexed at 4˚C for 15 m after the addition of 200 µl sterile glass beads, followed by centrifugation at 13500 rpm at 4 ºC for 10 m. The supernatant was retained and protein concentration was determined by Bradford assay (BioRad). Monoclonal anti-FLAG-M2-Peroxidase (HRP) (Sigma Aldrich, 1:2000) and anti-β actin (1:4000) were used for western blot.

Gene ontology analysis and identification of pathways that are potentially altered by treatment. Gene ontology analyses are performed via DAVID Bioinformatics tools (https://david.abcc.ncifcrf.gov), DiffBind, or WebGestalt (http://webgestalt.org).

Genomic association tests for correlation between DSBs and CFS cores and the "APH.breakome". The DSB regions with assigned replication timing indices (early vs. late, see Methods in main text) were compared to previously published finely mapped CFS core sequences (Savelyeva and Brueckner, 2014) and the "APH.breakome" (Crosetto et al., 2013), using the Genomic Association Tester (GAT) software (Heger et al., 2013). In all tests the DSBs were set as *segments* and the other datasets as *annotation,* with the genomic regions previously assigned with S50 values as *workspace* (*i.e.,* excluding those regions with S50 value of "NA") and default parameter for sampling rounds (--num-samples=1000).

REFERENCES

Alpatov, R., Lesch, B.J., Nakamoto-Kinoshita, M., Blanco, A., Chen, S., Stutzer, A., Armache, K.J., Simon, M.D., Xu, C., Ali, M.*, et al.* (2014). A chromatin-dependent role of the fragile X mental retardation protein FMRP in the DNA damage response. Cell *157*, 869-881.

Ashley, C.T., Jr., Wilkinson, K.D., Reines, D., and Warren, S.T. (1993). FMR1 protein: conserved RNP family domains and selective RNA binding. Science *262*, 563-566.

Bear, M.F., Huber, K.M., and Warren, S.T. (2004). The mGluR theory of fragile X mental retardation. Trends Neurosci *27*, 370-377.

Brown, V., Jin, P., Ceman, S., Darnell, J.C., O'Donnell, W.T., Tenenbaum, S.A., Jin, X., Feng, Y., Wilkinson, K.D., Keene, J.D.*, et al.* (2001). Microarray identification of FMRP-associated brain mRNAs and altered mRNA translational profiles in fragile X syndrome. Cell *107*, 477-487.

Chen, C.L., Rappailles, A., Duquenne, L., Huvet, M., Guilbaud, G., Farinelli, L., Audit, B., d'Aubenton-Carafa, Y., Arneodo, A., Hyrien, O.*, et al.* (2010). Impact of replication timing on non-CpG and CpG substitution rates in mammalian genomes. Genome research *20*, 447-457.

Ciaccio, C., Fontana, L., Milani, D., Tabano, S., Miozzo, M., and Esposito, S. (2017). Fragile X syndrome: a review of clinical and molecular diagnoses. Ital J Pediatr *43*, 39.

Coffee, B., Zhang, F., Ceman, S., Warren, S.T., and Reines, D. (2002). Histone modifications depict an aberrantly heterochromatinized FMR1 gene in fragile x syndrome. American journal of human genetics *71*, 923-932.

Cristini, A., Groh, M., Kristiansen, M.S., and Gromak, N. (2018). RNA/DNA Hybrid Interactome Identifies DXH9 as a Molecular Player in Transcriptional Termination and R-Loop-Associated DNA Damage. Cell Rep *23*, 1891-1905.

Crosetto, N., Mitra, A., Silva, M.J., Bienko, M., Dojer, N., Wang, Q., Karaca, E., Chiarle, R., Skrzypczak, M., Ginalski, K.*, et al.* (2013). Nucleotide-resolution DNA double-strand break mapping by next-generation sequencing. Nature methods *10*, 361-365.

Darnell, J.C., Van Driesche, S.J., Zhang, C., Hung, K.Y., Mele, A., Fraser, C.E., Stone, E.F., Chen, C., Fak, J.J., Chi, S.W.*, et al.* (2011). FMRP stalls ribosomal translocation on mRNAs linked to synaptic function and autism. Cell *146*, 247-261.

De Boulle, K., Verkerk, A.J., Reyniers, E., Vits, L., Hendrickx, J., Van Roy, B., Van den Bos, F., de Graaff, E., Oostra, B.A., and Willems, P.J. (1993). A point mutation in the FMR-1 gene associated with fragile X mental retardation. Nature genetics *3*, 31-35.

de Leon, J. (2003). Glucuronidation enzymes, genes and psychiatry. Int J Neuropsychopharmacol *6*, 57-72.

Docampo, M., Olubu, A., Wang, X., Pasinetti, G., and Dixon, R.A. (2017). Glucuronidated Flavonoids in Neurological Protection: Structural Analysis and Approaches for Chemical and Biological Synthesis. J Agric Food Chem *65*, 7607-7623.

Dominguez-Sanchez, M.S., Barroso, S., Gomez-Gonzalez, B., Luna, R., and Aguilera, A. (2011). Genome instability and transcription elongation impairment in human cells depleted of THO/TREX. PLoS genetics *7*, e1002386.

Entian, K.D., Schuster, T., Hegemann, J.H., Becher, D., Feldmann, H., Guldener, U., Gotz, R., Hansen, M., Hollenberg, C.P., Jansen, G.*, et al.* (1999). Functional analysis of 150 deletion mutants in Saccharomyces cerevisiae by a systematic approach. Molecular & general genetics : MGG *262*, 683-702.

Favorov, A., Mularoni, L., Cope, L.M., Medvedeva, Y., Mironov, A.A., Makeev, V.J., and Wheelan, S.J. (2012). Exploring massive, genome scale datasets with the GenometriCorr package. PLoS computational biology *8*, e1002529.

Feng, Y., Absher, D., Eberhart, D.E., Brown, V., Malter, H.E., and Warren, S.T. (1997). FMRP associates with polyribosomes as an mRNP, and the I304N mutation of severe fragile X syndrome abolishes this association. Molecular cell *1*, 109-118.

Fu, Y.H., Kuhl, D.P., Pizzuti, A., Pieretti, M., Sutcliffe, J.S., Richards, S., Verkerk, A.J., Holden, J.J., Fenwick, R.G., Jr., Warren, S.T.*, et al.* (1991). Variation of the CGG repeat at the fragile X site results in genetic instability: resolution of the Sherman paradox. Cell *67*, 1047-1058.

Garcia-Rubio, M., Aguilera, P., Lafuente-Barquero, J., Ruiz, J.F., Simon, M.N., Geli, V., Rondon, A.G., and Aguilera, A. (2018). Yra1-bound RNA-DNA hybrids cause orientation-independent transcription-replication collisions and telomere instability. Genes & development *32*, 965-977.

Giulivi, C., Napoli, E., Tassone, F., Halmai, J., and Hagerman, R. (2016). Plasma Biomarkers for Monitoring Brain Pathophysiology in FMR1 Premutation Carriers. Front Mol Neurosci *9*, 71.

Greenblatt, E.J., and Spradling, A.C. (2018). Fragile X mental retardation 1 gene enhances the translation of large autism-related proteins. Science *361*, 709-712.

Hamperl, S., Bocek, M.J., Saldivar, J.C., Swigut, T., and Cimprich, K.A. (2017). Transcription-Replication Conflict Orientation Modulates R-Loop Levels and Activates Distinct DNA Damage Responses. Cell *170*, 774-786 e719.

Hansen, R.S., Thomas, S., Sandstrom, R., Canfield, T.K., Thurman, R.E., Weaver, M., Dorschner, M.O., Gartler, S.M., and Stamatoyannopoulos, J.A. (2010). Sequencing newly replicated DNA reveals widespread plasticity in human replication timing. Proceedings of the National Academy of Sciences of the United States of America *107*, 139-144.

Hayward, B.E., Zhou, Y., Kumari, D., and Usdin, K. (2016). A Set of Assays for the Comprehensive Analysis of FMR1 Alleles in the Fragile X-Related Disorders. The Journal of molecular diagnostics : JMD *18*, 762-774.

Heger, A., Webber, C., Goodson, M., Ponting, C.P., and Lunter, G. (2013). GAT: a simulation framework for testing the association of genomic intervals. Bioinformatics *29*, 2046-2048.

Hein, M.Y., Hubner, N.C., Poser, I., Cox, J., Nagaraj, N., Toyoda, Y., Gak, I.A., Weisswange, I., Mansfeld, J., Buchholz, F., *et al.* (2015). A human interactome in three quantitative dimensions organized by stoichiometries and abundances. Cell *163*, 712-723.

Hellman, A., Rahat, A., Scherer, S.W., Darvasi, A., Tsui, L.C., and Kerem, B. (2000). Replication delay along FRA7H, a common fragile site on human chromosome 7, leads to chromosomal instability. Mol Cell Biol *20*, 4420-4427.

Hoffman, E.A., McCulley, A., Haarer, B., Arnak, R., and Feng, W. (2015). Break-seq reveals hydroxyurea-induced chromosome fragility as a result of unscheduled conflict between DNA replication and transcription. Genome research *25*, 402-412.

Khandjian, E.W., Huot, M.E., Tremblay, S., Davidovic, L., Mazroui, R., and Bardoni, B. (2004). Biochemical evidence for the association of fragile X mental retardation protein with brain polyribosomal ribonucleoparticles. Proceedings of the National Academy of Sciences of the United States of America *101*, 13357-13362.

Korb, E., Herre, M., Zucker-Scharff, I., Gresack, J., Allis, C.D., and Darnell, R.B. (2017). Excess Translation of Epigenetic Regulators Contributes to Fragile X Syndrome and Is Alleviated by Brd4 Inhibition. Cell *170*, 1209-1223 e1220.

Krawczun, M.S., Jenkins, E.C., and Brown, W.T. (1985). Analysis of the fragile-X chromosome: localization and detection of the fragile site in high resolution preparations. Human genetics *69*, 209-211.

Landolfi, A., Troisi, J., Savanelli, M.C., Vitale, C., Barone, P., and Amboni, M. (2017). Bisphenol A glucuronidation in patients with Parkinson's disease. Neurotoxicology *63*, 90-96.

Le Beau, M.M., Rassool, F.V., Neilly, M.E., Espinosa, R., 3rd, Glover, T.W., Smith, D.I., and McKeithan, T.W. (1998). Replication of a common fragile site, FRA3B, occurs late in S phase and is delayed further upon induction: implications for the mechanism of fragile site induction. Human molecular genetics *7*, 755-761.

Li, Y., Stockton, M.E., Eisinger, B.E., Zhao, Y., Miller, J.L., Bhuiyan, I., Gao, Y., Wu, Z., Peng, J., and Zhao, X. (2018). Reducing histone acetylation rescues cognitive deficits in a mouse model of Fragile X syndrome. Nature communications *9*, 2494.

Murano, I., Kuwano, A., and Kajii, T. (1989). Fibroblast-specific common fragile sites induced by aphidicolin. Human genetics *83*, 45-48.

Nakamoto, M., Nalavadi, V., Epstein, M.P., Narayanan, U., Bassell, G.J., and Warren, S.T. (2007). Fragile X mental retardation protein deficiency leads to excessive mGluR5-dependent internalization of AMPA receptors. Proceedings of the National Academy of Sciences of the United States of America *104*, 15537-15542.

Niere, F., Wilkerson, J.R., and Huber, K.M. (2012). Evidence for a fragile X mental retardation protein-mediated translational switch in metabotropic glutamate receptor-triggered Arc translation and long-term depression. The Journal of neuroscience : the official journal of the Society for Neuroscience *32*, 5924-5936.

Palakodeti, A., Han, Y., Jiang, Y., and Le Beau, M.M. (2004). The role of late/slow replication of the FRA16D in common fragile site induction. Genes, chromosomes & cancer *39*, 71-76.

Pieretti, M., Zhang, F.P., Fu, Y.H., Warren, S.T., Oostra, B.A., Caskey, C.T., and Nelson, D.L. (1991). Absence of expression of the FMR-1 gene in fragile X syndrome. Cell *66*, 817-822.

Prado, F., and Aguilera, A. (2005). Impairment of replication fork progression mediates RNA polII transcription-associated recombination. The EMBO journal *24*, 1267-1276.

Santoro, M.R., Bray, S.M., and Warren, S.T. (2012). Molecular mechanisms of fragile X syndrome: a twenty-year perspective. Annual review of pathology *7*, 219-245.

Sanz, L.A., Hartono, S.R., Lim, Y.W., Steyaert, S., Rajpurkar, A., Ginno, P.A., Xu, X., and Chedin, F. (2016). Prevalent, Dynamic, and Conserved R-Loop Structures Associate with Specific Epigenomic Signatures in Mammals. Molecular cell *63*, 167-178.

Savelyeva, L., and Brueckner, L.M. (2014). Molecular characterization of common fragile sites as a strategy to discover cancer susceptibility genes. Cellular and molecular life sciences : CMLS *71*, 4561-4575.

Sethna, F., Moon, C., and Wang, H. (2014). From FMRP function to potential therapies for fragile X syndrome. Neurochemical research *39*, 1016-1031.

Sheridan, S.D., Theriault, K.M., Reis, S.A., Zhou, F., Madison, J.M., Daheron, L., Loring, J.F., and Haggarty, S.J. (2011). Epigenetic characterization of the FMR1 gene and aberrant neurodevelopment in human induced pluripotent stem cell models of fragile X syndrome. PloS one *6*, e26203.

Siomi, H., Choi, M., Siomi, M.C., Nussbaum, R.L., and Dreyfuss, G. (1994). Essential role for KH domains in RNA binding: impaired RNA binding by a mutation in the KH domain of FMR1 that causes fragile X syndrome. Cell *77*, 33-39.

Verkerk, A.J., Pieretti, M., Sutcliffe, J.S., Fu, Y.H., Kuhl, D.P., Pizzuti, A., Reiner, O., Richards, S., Victoria, M.F., Zhang, F.P.*, et al.* (1991). Identification of a gene (FMR-1) containing a CGG repeat coincident with a breakpoint cluster region exhibiting length variation in fragile X syndrome. Cell *65*, 905-914.

Wang, L., Darling, J., Zhang, J.S., Huang, H., Liu, W., and Smith, D.I. (1999). Allele-specific late replication and fragility of the most active common fragile site, FRA3B. Human molecular genetics *8*, 431-437.

Wongsurawat, T., Jenjaroenpun, P., Kwoh, C.K., and Kuznetsov, V. (2012). Quantitative model of R-loop forming structures reveals a novel level of RNA-DNA interactome complexity. Nucleic acids research *40*, e16.

Yu, S., and Lemos, B. (2016). A Portrait of Ribosomal DNA Contacts with Hi-C Reveals 5S and 45S rDNA Anchoring Points in the Folded Human Genome. Genome biology and evolution *8*, 3545-3558.

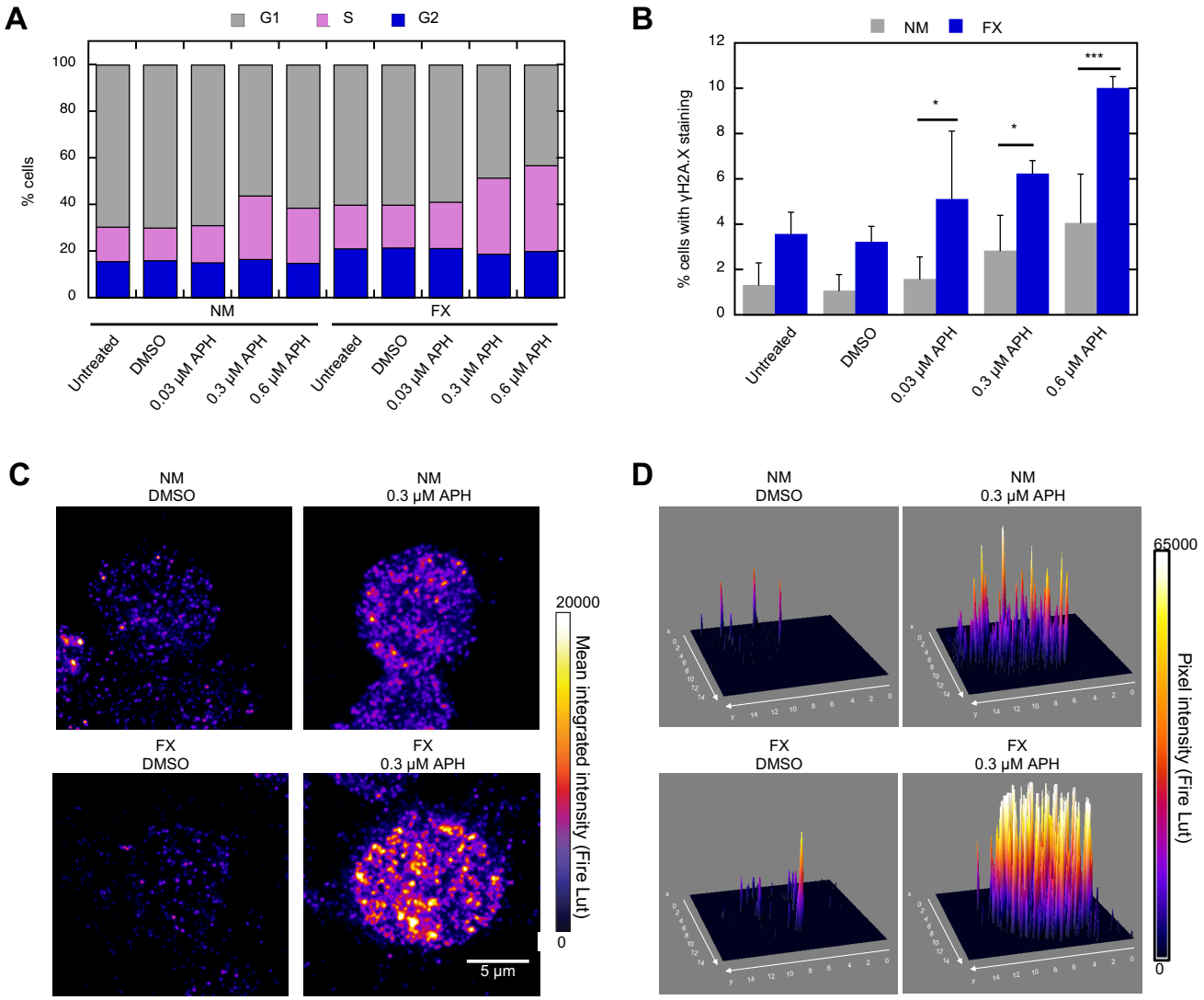

Figure 1. **Fragile X cells show elevated DNA damage in vivo.** (**A**) Flow cytometry analysis shows that APH treatment enriches for cells in S phase. Three independent experiments were performed and one representative experiment is shown. (**B**) Flow cytometric sorting of γ-H2A.X-positive cells under APH-induced replication stress. Bars indicate mean and standard deviation for three independent experiments (except for 0.6 μM APH for which two experiments were performed). Two-way ANNOVA test p values: *p<0.05, ***p<0.001, ****p<0.0001. Ten thousand cells were analyzed in each flow experiment. (**C**) Single cell view of γ-H2A.X foci distribution, expressed as mean integrated density (FIRE, LUT) for the indicated samples, in NM and FX cells. (**D**) 3D surface plots of γ-H2A.X intensity distribution in the cells from (**C**), x and y axes are in microns and the z axis is expressed as pixel intensity after thresholding at each focus (FIRE, LUT), in NM and FX cells.

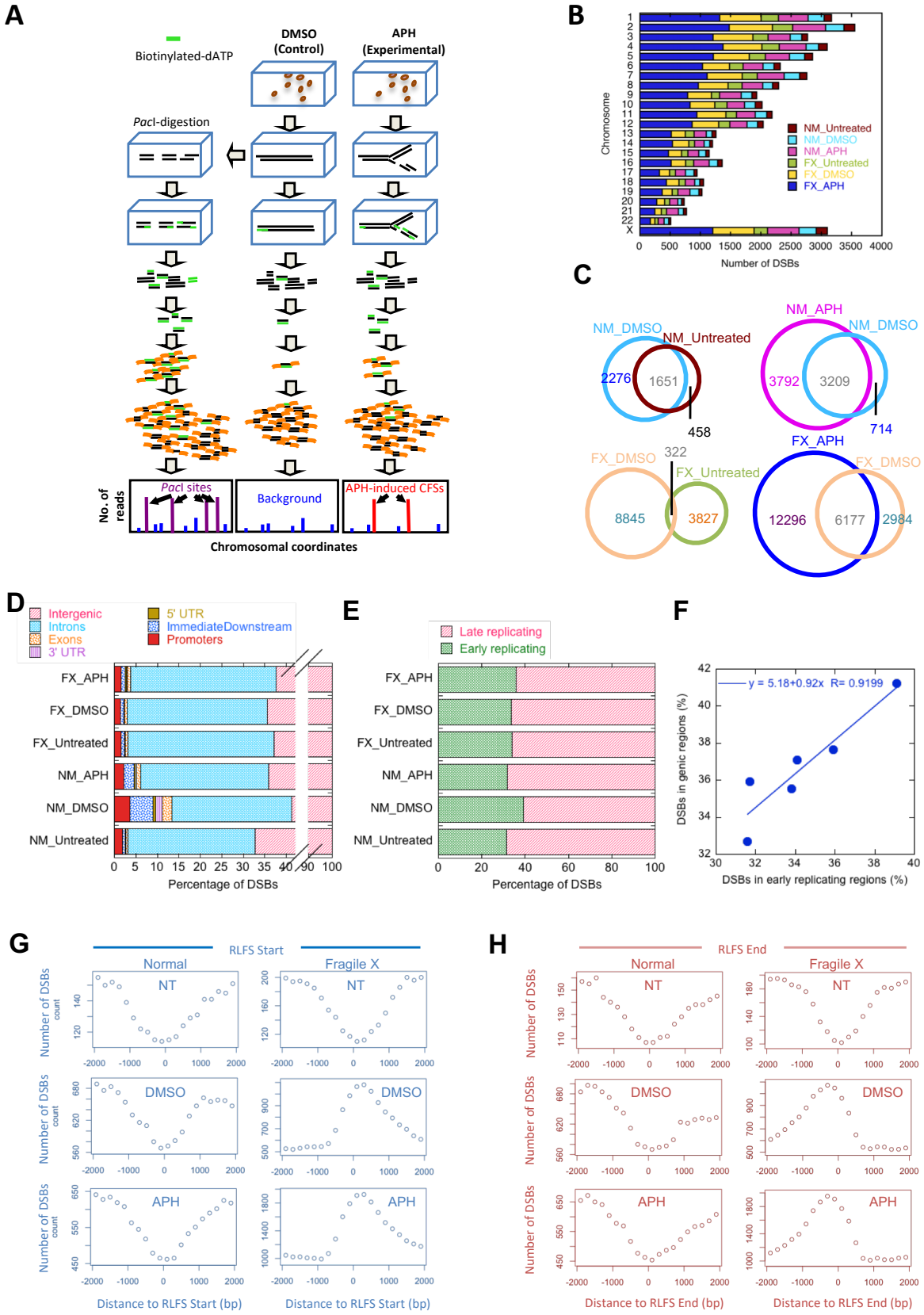

Figure 2. Break-seq mapping shows high level of DSBs in FX cells and drug-induced DSBs in FX correlate with RLFSs. **(A)** Break-seq methodology. (**B**) Chromosomal distribution of the number of DSBs in the indicated categories. **(C)** Venn diagrams showing the concordance between samples of different treatments. FX cells show "reprogramming" of drug-induced DSBs compared to those in the untreated cells. **(D)** Distribution of DSB peaks relative to genes in the indicated samples. Genic features include introns, exons, 5'- and 3'-UTRs, promoters, and the immediately downstream (<1kb from the 3'-UTR) regions (ImmediateDownstream). (**E**) Distribution of DSBs in early vs. late replicating regions of the genome, as defined by Hansen RS et al, in the indicated samples. See Methods for details. (**F**) Correlation between the percentage of DSBs associated with genes and the percentage of DSBs with early replication timing. Aggregated DSBs from the indicated samples around the start **(G)** or the end **(H)** of R loop forming sites (RLFSs) in a 4000 bp window centering on the RLFS.

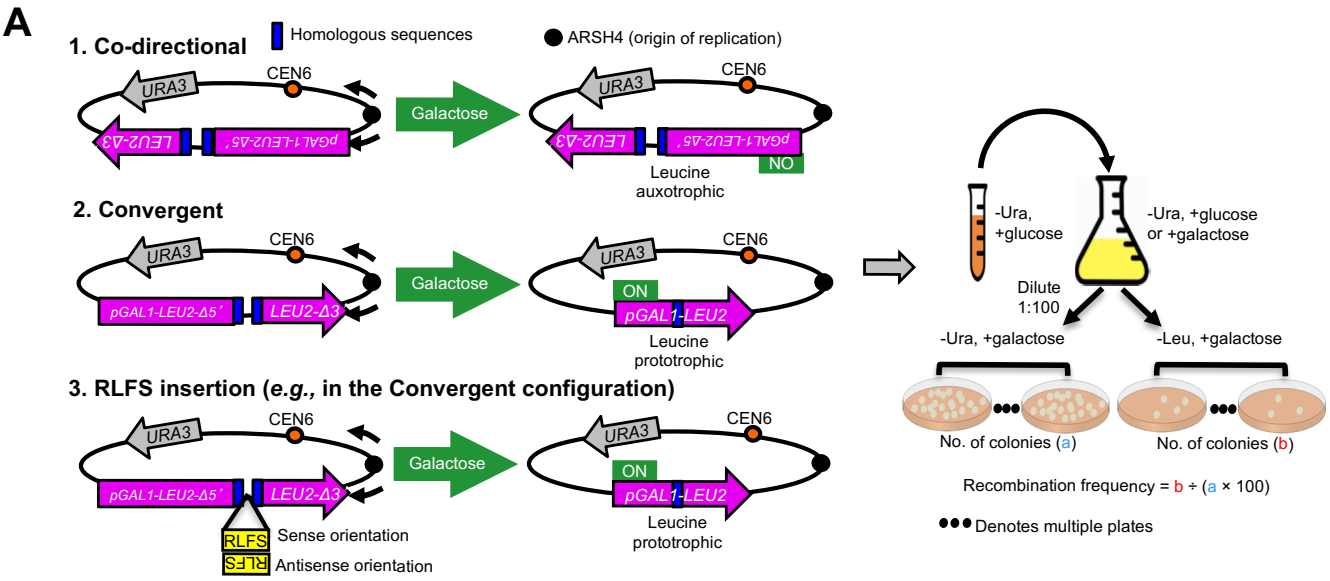

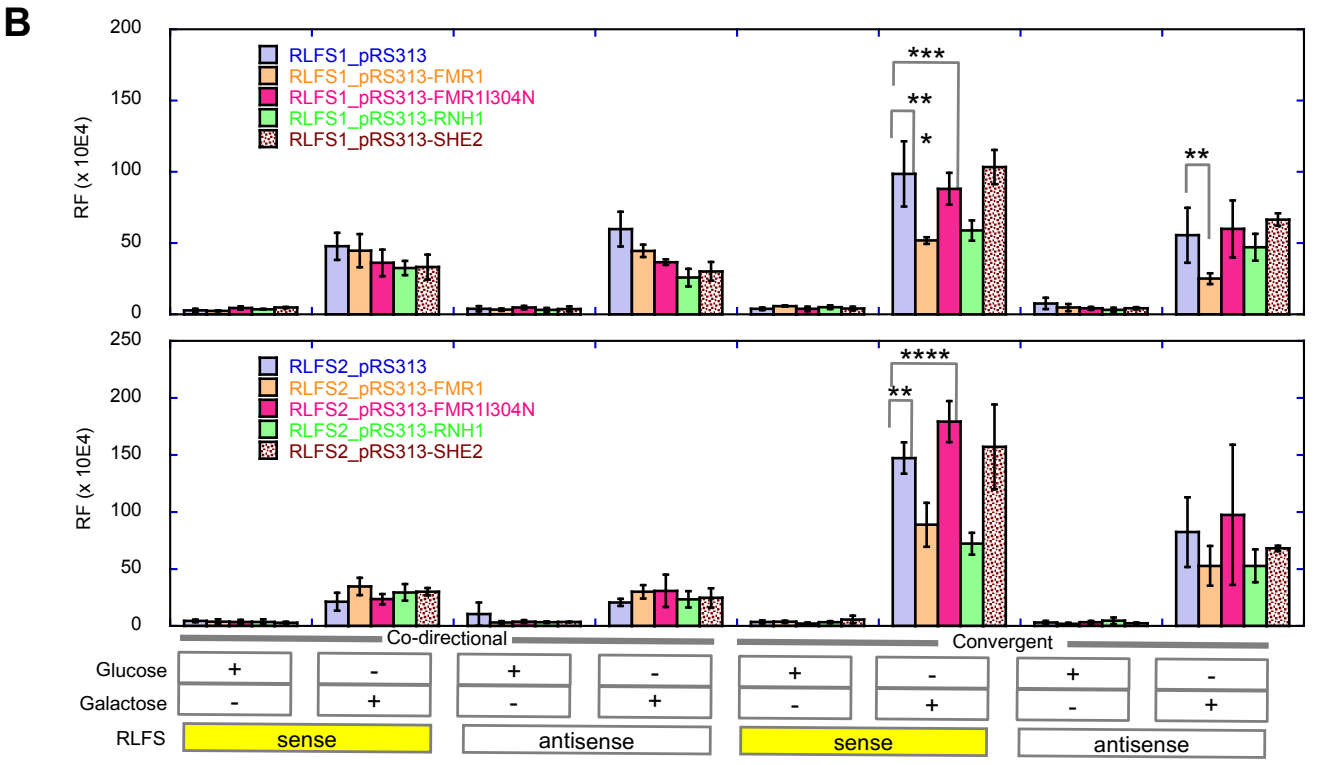

Figure 3. **FMRP expression suppresses RLFS-induced DSB formation.** (**A**) A non-functional *LEU2* marker containing two inserted direct repeats and driven by a galactose-inducible *GAL1* promoter was placed next to an origin of replication (*ARSH4*) such that the direction of transcription is convergent or codirectional with respect to the direction of the proximal replication fork. Upon galactose induction, convergent replication and transcription would induce DSBs and homologous recombination repair to generate a functional *LEU2*, resulting in leucine prototrophy. Two RLFSs from the human genome (RLFS1-1 from the promoter of *FMR1* and RLFS-2 from intron 5 of Fragile Histidine Triad) were inserted between the direct repeats to test for enhanced DSB and recombination. A non-RLFS sequence without predicted R-loop forming propensity and with similar G-richness in both strands served as control. All sequences were similar in size (~500 bp). The RLFSs were inserted in the sense or anti-sense orientation with respect to *LEU2* transcription (*i.e.*, G-rich strand on the non-template or template strand, respectively), with the sense orientation expected to preferentially induce R-loop formation. The control sequence was also inserted in two orientations and no difference in RF was observed between them (Fig. S3C). RF is calculated based on the percentage of leucine prototrophs after plating. (**B**) The effect of ectopitc expression of indicated genes on the pRS313 plasmid, under the CMV promoter, on RLFS-induced RF. Bars indicate mean and standard deviation between biological replicates (n=3). P values for Two-way ANNOVA test: *p<0.05,***p<0.001,****p<0.0001. See Figure S3 for additional control experiments.

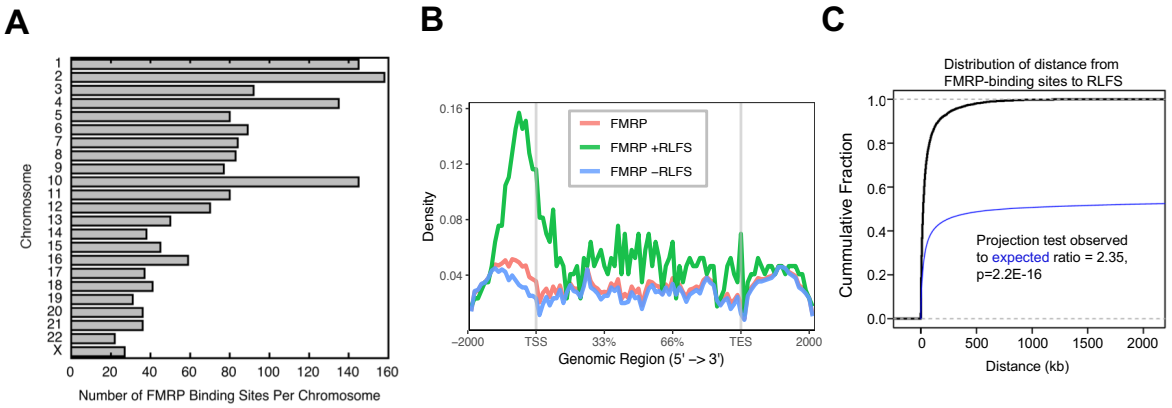

D

Biological process	P-value	FDR
Flavonoid metabolic process	0.00E+00	2.26E-02
Lamellipodium organization	1.33E-03	3.26E-01
Second-messenger-mediated signaling	3.38E-03	3.33E-01
Response to xenobiotic stimulus	3.63E-03	3.60E-01
Cell communication by electrical coupling	4.08E-03	3.29E-01
Sodium ion transport	5.41E-03	3.15E-01
Drug metabolic process	5.47E-03	3.49E-01
Acute inflammatory response	8.83E-03	3.06E-01
Isoprenoid metabolic process	9.79E-03	6.02E-01
Glutamate receptor signaling pathway	1.65E-02	6.50E-01

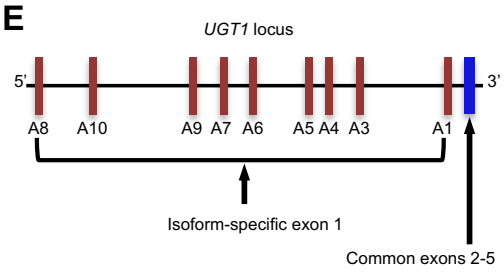

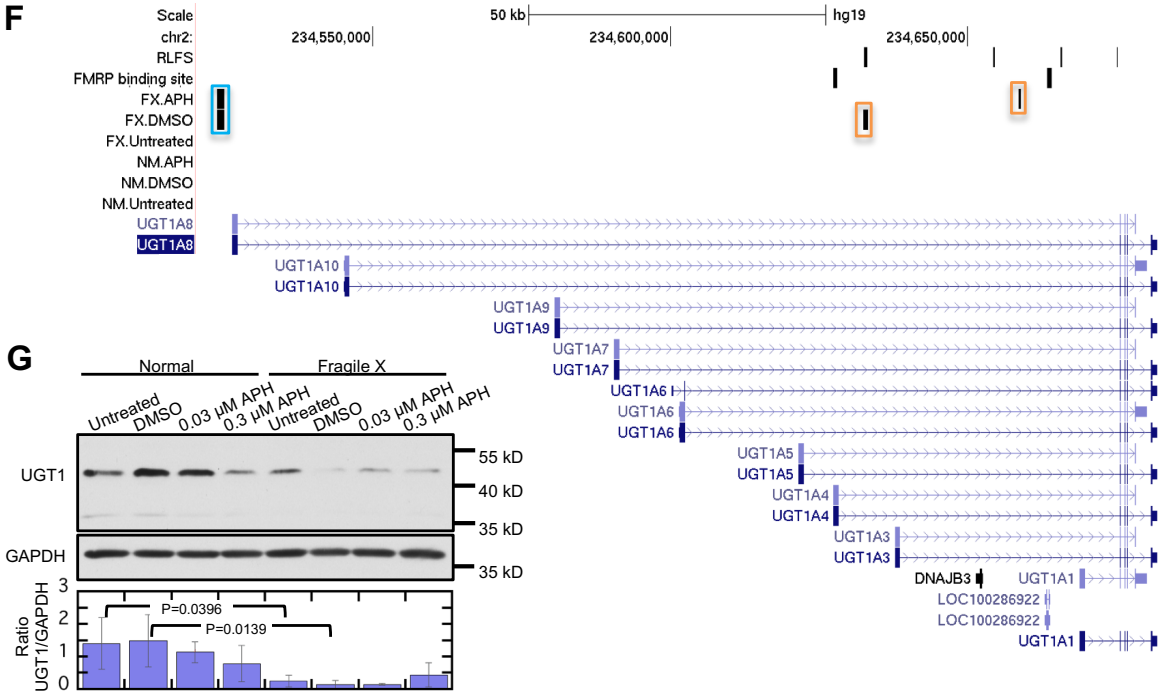

Figure 4. Analysis of chromatin binding sites of FMRP. (**A**) Distribution of the number of FMRP binding sites (FBSs) per chromosome. (**B**) Distribution of the FMRP-binding sites inside genic regions, and in regions upstream of TSS (Transcription Start Sites) and TES (Transcription End Sites). Red, green and blue lines represent distribution of 5238 FBSs, 283 FBSs with overlapping RLFS and 4955 FBSs without overlapping RLFS, respectively. (**C**) Observed absolute distance between FBSs and RLFSs (blue) compared to the expected distance if uncorrelated (black line). (**D**) Biological processes derived from WebGestalt (WEB-based GEne SeT AnaLysis Toolkit) that are enriched for those genes bound by FMRP; FDR, false discovery rates. (**E**) Schematic representation of UGT1A subfamily alternative splicing isoforms. (**F**) UCSC genome browser screen shot of FX-specific DSBs shown as vertical bars (upstream of the gene, cyan box; in the intron preceding the common exons 2-5, orange boxes) in *UGT1* family genes. (**G**) Representative Western blots of UGT1 protein expression with GAPDH as control and quantification using ratio of UGT1 to GAPDH derived from three biological replicates. Error bars denote standard deviation. P values that are < 0.05 from Two-way ANNOVA test are shown.

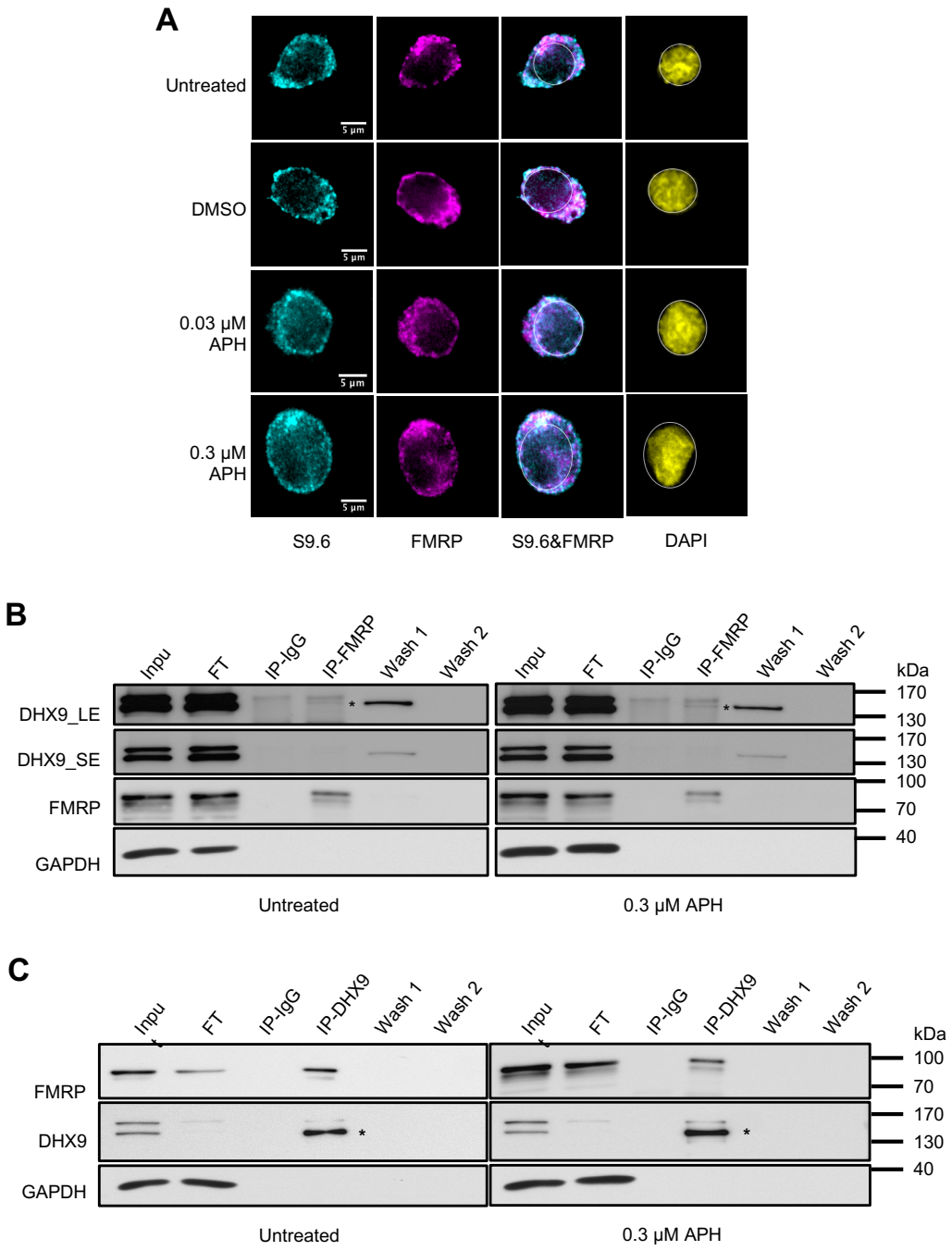

Figure 5. FMRP is co-localized to R-loop forming sites and co-immunoprecipitates with DHX9. (**A**) Co-localization of FMRP and RNA:DNA hybrids. Immunofluorescence images of untreated, DMSO- and APH-treated NM cells co-stained for RNA:DNA hybrids (cyan), FMRP (magenta) and nucleus (yellow, outlined). Immuno-staining is shown in a single Z-plane. Scale bar, 5 μm. (**B**) Co-immunoprecipitation of FMRP and DHX9 using the anti-FMRP monoclonal antibody (Covance) to pull down FMRP and immunoblotted for both FMRP and DHX9. GAPDH served as negative control. The asterisks indicate the lower band of a doublet signal in the "IP-FMRP" lanes is the DHX9 protein, which is present in the FMRP-immunoprecipitated complex and absent in the IgG-precipitated control complex ("IP-IgG" lanes). Substantial fraction of DHX9 is also present in the first wash (Wash 1) of the immunoprecipitate, likely due to the abundance of DHX9. LE, long exposure; SE, short exposure. (**C**) Reciprocal immunoprecipitation using anti-DHX9 and blotted for both DHX9 and FMRP, with GAPDH serving as negative control.

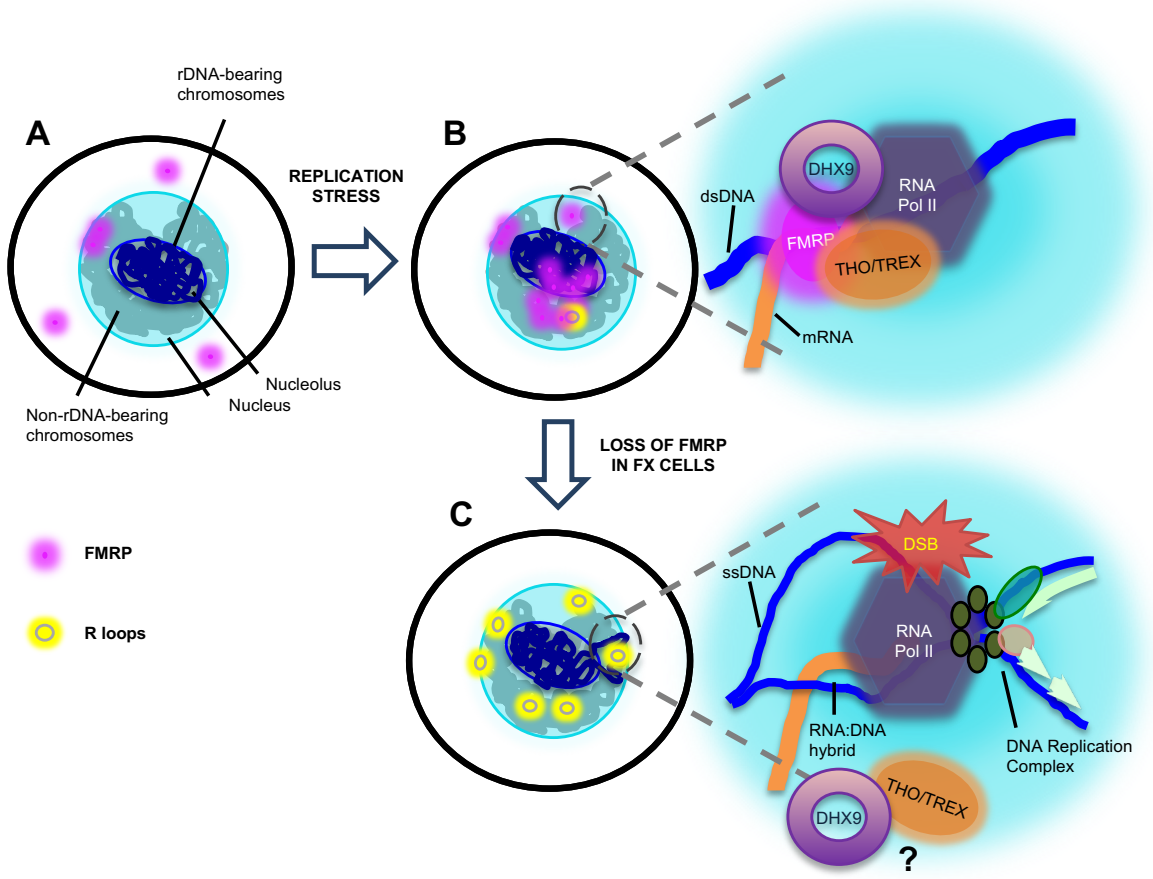

Figure 6. Proposed model of a novel FMRP function in the nucleus. (A) Illustration of a normal lymphoblastoid cell without any treatment, showing FMRP in the cytoplasm and in the nuclear periphery possibly engaged in mRNA transport. **(B)** Under replication stress, FMRP localizes to the center of the nucleus at R-loop formation sites in genes induced by DMSO and APH. At the junction of convergent replication and transcription, FMRP in conjunction with DHX9 and possibly the THO/TREX complex is involved in R-loop removal and avoidance of a deleterious collision (inset). dsDNA, double-stranded DNA. **(C)** In FX cells increased protein synthesis rate demands high level rRNA production on the rDNA-bearing chromosomes, which in turn causes increased level of (Pol II) transcription elsewhere on these chromosomes, represented by the chromosome loops tethered to the nuclear pores for active transcription. Absence of FMRP permits stable R-loop formation and DSBs upon collision of replication and transcription (inset). The fate of the THO/TREX complex in this context remains to be determined. ssDNA, single-stranded DNA.

SUPPLEMENTAL INFORMATION

SUPPLEMENTAL METHODS

Break-seq

***Break-seq library construction*.** Break-seq procedures were as described previously with modifications (Hoffman et al., 2015). $5x10^6$ cells were embedded into 0.5% Incert low-melting point agarose in PBS and cast into plugs. The agarose plugs were then incubated at 50ºC overnight in 6 ml of lysis buffer (0.5 M EDTA, 1% Sarkosyl, 200 µg/ml Proteinase K). The DNA in the agarose plugs was then end-labeled in-gel using the End-It Kit (Epicentre) with biotinylated dNTP mix (1 mM dTTP, dCTP, dGTP, 0.84 mM dATP, 0.16 mM Biotin-14-dATP). Plugs were then treated with β-Agarase (NEB) to digest agarose and release DNA. DNA sample was then sonicated using a Covaris M220 using the snap-cap DNA 300 bp shearing protocol. DNA was then processed using a PCR Cleanup Kit (Qiagen) and run on agarose gel to verify the fragmentation pattern of DNA and quantified on a Nanodrop. 10-11 µg of DNA was then end repaired (Epicentre) and purified by the PCR Cleanup Kit (Qiagen). The DNA was then A-tailed by A-tail Kit (NEB) or Klenow exo- (NEB E6054A) and purified by PCR Clean-up Kit (Qiagen), followed by quantification on a Nanodrop. M270 Dynabeads (Life Technologies) were used to purify biotinylated DNA. The amount of DNA bound to beads was calculated by measuring the quantity of DNA in the flow through. DNA-bound beads were then resuspended in ligation mix containing Illumina adaptors (50 µM adaptor-1, 50 µM adaptor-2, 1x T4 ligase buffer, 3 µl T4 DNA ligase) and incubated overnight at room temperature on a roller. 400 ng of DNA bound to beads was used for PCR amplification using KAPA Hotstart Ready Mix (KAPA). Each sample was given a specific index primer for multiplexing. PCR product was then run on agarose gel to verify amplification and quantity. AMPure beads (Agencourt) were used to remove free adaptors and the final product was analyzed on agarose gel. Break-seq libraries were sequenced on Illumina Hi-Seq 2500 with 100 or 150 bp paired-end reads, followed by Break-seq data analysis. Adaptor sequences and index primer sequences were previously described (Hoffman et al., 2015).

Break-seq DSB peak identification. Raw sequence reads were obtained from Illumina Hi-seq 2500 and then aligned to the UCSC human genome assembly, GRCh37/hg19

(http://hgdownload.soe.ucsc.edu/goldenPath/hg19/bigZips/), using Bowtie 2 (http://bowtie-bio.sourceforge.net/bowtie2/index.shtml) in the "--*local"* mode. The PCR duplicate reads were removed using Picard MarkDuplicates (http://broadinstitute.github.io/picard). The non-redundant mapped sequence reads were sorted and then converted to BAM files using SAMtools (Li et al., 2009) (http://samtools.sourceforge.net/) and subjected to subsequent processing with Model-based Analysis for ChIP-seq (MACS version 2.1.1, https://pypi.python.org/pypi/MACS2) using two-sample analysis between break-seq samples (treatment) and whole genome sequencing data (control) using the *callpeak* function in MACS2 with a p value <1e-5. For identification of *Pac*I-digested breaks, DSB peaks with perfect match to *Pac*I motif (TTAATTAA) were mapped onto the hg19 reference genome with Bowtie. *IntersectBED* function from BEDtools (Quinlan and Hall, 2010) was then used to find overlap between *Pac*I motif sites and peaks identified through MACS2. These overlapping peaks were considered *Pac*I sites found in the Break-seq sample.

Random permutation tests for identification of PacI sites. The *shuffleBed* function in BEDtools was used to randomly permute the genomic locations of DSBs identified as *Pac*I sites with default parameters to generate randome genomic locations as a null distribution, preserving the size of DSBs and number of DSBs per chromosome. The fraction of sequences containing *Pac*I motif was calculated. One thousand iterations of this process was performed. The distribution of the *Pac*I-positive fractions was then compared to that from the experimental dataset and One Sample Student's t-test was performed.

Break-seq library complexity calculation and identification of consensus DSB peaks in replicate experiments. All biological replicates for each sample (strain/treatment combination) were pooled for assessement of library complexity by preseq (Daley and Smith, 2013). All 23 Break-seq peak files were analyzed in DiffBind (Ross-Innes et al., 2012) for consensus DSB peak identification. Consensus DSB peaks were defined as those that appear in at least two replicate experiments, regardless of the total number of replicates, for each sample (cell line/treatment). Aphidicolin-treated samples (0.03 μM and 0.3 μM) were combined to form a composite APH-treated sample, for both NM and FX cells, and consensus DSB peaks were then extracted similarly as described.

Correlation between DSBs and other genomic features. The association between DSBs and other genomic features including RLFSs and DRIP-seq signals was determined using the *bedtools annotate* function. Multiple data sets of DRIP-seq were concatenated (*cat GSE70189_NT2_DRIPc_peaks GSM1720615_NT2_DRIP_1_peaks GSM1720616_NT2_DRIP_2_peaks GSM1720617_NT2_DRIP_RNaseA_peaks GSM1720618_NT2_DRIP_RNaseH_peaks GSM1720619_K562_DRIP_peaks.clip > composite.DRIP*), sorted (*sort -k1,1 -k2,2n composite.DRIP > composite.DRIP.sorted*) and then merged into a composite data set using the *bedtools merge* function (*bedtools merge –i composite.DRIP.sorted > composite.DRIP.sorted.merged*). The significance of the association or p value was calculated using the fisher exact test (*fisher*) in BEDtools. Relative distance between DSBs and RLFSs was calculated using *bedtools reldist* function.

ChIP-seq

Cell collection. GM06990 and GM03200 cells were grown to log phase with a viability >90%. Cell fixation, harvest and IP were conducted according to Richard Myers lab ChIP-seq protocol. Briefly, cells were fixed with 1% formaldehyde for 10 m at room temperature and then blocked with 0.125 M glycine. Cells were then washed twice with cold PBS. Cells were collected at $2x10^7$ cells per ChIP reaction, snap frozen in liquid nitrogen and stored at -80ºC untill further use.

Immunoprecipitation. Cells were thawed on ice with 1 ml Farham's lysis buffer (5 mM PIPES pH 8.0, 85 mM KCl, 0.5% NP-40, Halt protease inhibitor cocktail (Thermo Scientific)) for 5 m. Nuclei were prepared by centrifuging the lysate at 2000 rpm for 5 m. The nuclear pellet was resuspended in 300 µl RIPA (1x PBS, 1% NP-40, 0.5% sodium deoxycholate, 0.1% SDS, Halt protease inhibitor cocktail). Samples were sonicated in a Bioruptor (Diagenode) at high setting for a total time of 40 m with 30 s ON and 30 s OFF at 4°C. The sonicated mixture was centrifuged at 13,500 rpm for 15 m at 4°C and the volume of supernatant was adjusted to 1 ml with RIPA buffer. One hundred µl of this mixture was set aside as "input" and the remaining nuclear fraction was used for immunoprecipitation. Both aliquots were snap frozen in liquid nitrogen and stored at -80°C until ready for immunoprecipation. Ten µg of monoclonal anti-FMRP antibody (Covance, now Biolegend, Cat#MMS-5231) was conjugate with M280 Dynabeads sheep anti-mouse IgG (Life Technologies). The thriced washed beads (with

PBS/BSA) were incubated with 900 µl sonicated nuclear fraction overnight at 4°C with agitation. The beads were then washed 5 times with cold LiCl wash buffer (100 mM Tris pH7.5, 500 mM LiCl, 1% NP-40, 1% sodium deoxycholate), followed by a single wash in TE (10 mM Tris-HCl pH7.5, 0.1 mM EDTA). The immunoprecipitates were eluted with 200 µl of IP elution buffer (1% SDS, 0.1 M $NaHCO_3$) at 65°C for 2 h with vortexing every 30 m. The 100 µl "input" was thawed and together with the eluted immunoprecipitates were reverse-crosslinked at 65°C overnight. The samples were then used for ChIP-seq library construction.

Library preparation. DNA was purified from all samples (input and immunoprecipitates described above) using Qiagen PCR clean-up kit and then end-repaired in a 100 µl reaction (1x End-repair buffer, 250 µM dNTP mix, 1 mM ATP, and 3 µl End-It Enzyme (Epicentre)) for 45 m at room temperature. Labeled DNA was purified using Qiagen PCR clean-up kit, A-tailed using Klenow(exo-), purified again with Qiagen PCR clean-up kit, and ligated to Ilumina adaptors using the same conditions as described for Break-seq. Ligated DNA was purified with Qiagen PCR clean-up kit and amplified by PCR using index primers (98°C, 5 m; 18 cycles of 98°C, 20 s; 65°C, 15 s; 72°C, 1 m; followed by 1 cycle of 72°C, 5 m). The PCR products were purified by AmPure beads (AgenCourt) to remove free adaptors.

ChIP-seq data analysis. Raw sequence reads were aligned to hg19 by Bowtie2 the same as for Break-seq data. The non-redundant mapped sequence reads were used for peak calling by Model-based Analysis for ChIP-seq (MACS version 1.4.1). Identification of FMRP-binding sites was done using two-sample analysis between ChIP samples from GM06990 (treatment) and GM03200 (control) with the *callpeak* function and applying a p value < 1E-05.

ChIP-qPCR. ChIP was conducted as before, we additionally used IgG along with FMRP antibody as a control in GM06990 cells only. After immunoprecipitation and DNA isolation, the ChIP'ed DNA and the input DNA was diluted 1:10 in water. The PCR reaction was carried out in 10 µl volume. 5 µl of iTaq Universal SYBR Supermix (BioRad), 300 nm of forward and reverse primers (Supplemental Table S6), 3 µl DNA and water made up the reaction mixture. CFX connect real time system (BioRad) was used for qPCR with the following thermal cycling protocol; 95ºC for 30 s, cycle: 95ºC for 10 s and 58ºC for 30 s. This was followed by melt curve analysis from 65ºC to 95ºC by an increment of 0.5ºC for 5 s. 45 cycles were used for every reaction.

SUPPLEMENTAL RESULTS AND DISCUSSION

Break-seq proof-of-principle experiments and analysis pipeline.

As a proof-of-principle we mapped DSBs produced by *in vitro Pac*I-digestion of DNA from FX cells treated with DMSO or 0.03 μM APH (Supplemental Fig. S1A). More than 96% of DSBs mapped in these two samples correspond to a known *Pac*I site ($p < 2.2e-16$ in random permutation tests with 1000 iterations, see Methods), with 86% concordance between them (Supplemental Table S1). Of the 151,583 *Pac*I sites in the human hg19 genome, 84,672 (56%) and 89,199 (59%) were mapped in the DMSO and APH samples, respectively. These results provided a benchmark for Break-seq with > 97% specificity and > 56% sensitivity (the in-gel digestion efficiency of *Pac*I was ~70% based on Southern blot analysis (data not shown), suggesting a true Break-seq sensitivity of ~80%) . Break-seq library qualities were assessed for read classification (Supplemental Fig. S1B&C) and library complexity (Supplemental Fig. S1D). All Break-seq libraries did not appear to be saturated, but at the current sequencing depth recurrent DSBs were identified. For each strain/treatment combination, *e.g.*, "FX_0.03 μM APH", *consensus DSBs* from at least two replicate experiments, regardless of the total number of replicates, were derived (Supplemental Table S2). The DSBs from 0.03 μM and 0.3 μM APH-treated samples were further pooled into a composite dataset of "APH-treated DSBs", for each cell line, followed by comparison with the DMSO-treated control to identify DSBs shared by DMSO- and APH-treatment as well as those specific to each treatment (Supplemental Fig. S2A&B, Supplemental Table S2). The concordance of DSB peaks between FX and NM cells was determined (Supplemental Fig. S2C).

Comparison between DSBs in this study with previously published CFS cores and the "APH.breakome".

APH-induced chromosome breakage defines common fragile sites (CFSs) (Glover et al., 1984). CFSs are also characterized by late replication timing (Hellman et al., 2000; Le Beau et al., 1998; Palakodeti et al., 2004; Wang et al., 1999). We systematically compared the APH-induced DSBs mapped in our study to fourteen reported CFS core sequences (Savelyeva and Brueckner, 2014) and a list of DSBs mapped by a genome-wide technique named BLESS in APH-treated HeLa cells (henceforth "APH.breakome" as named by Crosetto et al) (Crosetto et al., 2013). Indeed,

we observed significant correlation between replication stress-induced DSBs in NM and FX cells with the "APH.breakome" ($p < 0.001$, Supplemental Fig. S7A&B). Moreover, the concordant DSBs (those that were shared between our data and the "APH.breakome") were associated with the late replicating regions for both NM and FX cells. This is consistent with the notion that delayed replication timing of intrinsically difficult-to-replicate sequences are prone to DSBs. In addition, the stress-induced DSBs in FX cells were also associated with early replicating regions (Supplemental Fig. S7C&D), which tend to be transcriptionally active and are prone to replication-transcription conflict. However, we did not find significant ($p < 0.001$) correlation between DSBs in any sample with the CFS cores (data not shown). Closer scrutiny of the experimental conditions in CFS studies allowed us to conclude that this apparent discrepancy stemmed from the differential usage of organic solvent for APH, *i.e.*, ethanol vs. DMSO.

Since the first documented usage of ethanol and DMSO as the solvent for APH and the induction of CFSs (Glover et al., 1984), different laboratories have taken to use either solvent for their studies. Direct comparison between these two solvents in CFS induction has only been documented—to the best of our knowledge—in a single study using two subjects (Kuwano and Kajii, 1987). This study demonstrated that increasing concentrations of ethanol, but not DMSO, synergistically increased APH-induced CFSs. It also showed that ethanol treatment alone induced CFS formation at a frequency of 2-9% when administered at a range between 0.02% and 1%. Unfortunately, the effect of DMSO alone on CFS induction was not measured. Our study suggests that DMSO, at least when administered at 0.02%, enhances DSB formation (see more below) compared to untreated cells. Nevertheless, the study by Kuwano and Kajii suggested that ethanol and DMSO have different impact on CFS formation, particularly in the context of APH treatment. Among the studies from which the CFS core sequences were derived and compiled by Savelyeva and Brueckner (Savelyeva and Brueckner, 2014) (Table 1 therein), all but one study used ethanol as the solvent. The study by Zimonjic et al (reference 51 therein) used either ethanol or DMSO to map the FRA3B site and the results were an undifferentiated mixture. In contrast, our study as well as the BLESS study (Crosetto et al., 2013) used DMSO as the solvent for APH. Therefore, it appears that CFS formation is a product of both APH treatment and other undefined cellular effects by ethanol or DMSO, rendering comparison between studies that employ differential usage of these solvents rather tenuous.

Our study revealed that DMSO sensitizes RLFS regions for DSBs in both NM and FX cells (Table 1). DMSO is one of the most common solvents for organic compounds and facilitates the delivery of drugs across cellular membranes. It is also known as an antioxidant with a protective role for human tissues by interacting with the hydroxyl group on various substances. Its protective role is exemplified in its ability to reduce the damaging effect on DNA molecules by radiation. However, depending on the concentration and cellular context DMSO can function as an antioxidant or a pro-oxidant (Kang et al., 2017; Liu et al., 2001; Perez-Pasten et al., 2006; Sadowska-Bartosz et al., 2013). Moreover, its potential genome-damaging effect has not yet been evaluated in mammalian cells to the best of our knowledge. Fortuitously we discovered that 0.02% DMSO (the concentration at which we used to dissolve APH) can cause chromosome breakage in human lymphoblasts through an unknown mechanism. We assume this genotoxic effect is not tissue-specific. Thus, it is imperative to understand the full cellular and genomic impact by DMSO to inform therapeutic treatment involving DMSO as a solvent.

REFERENCES FOR SUPPLEMENTAL INFORMATION

Alpatov, R., Lesch, B.J., Nakamoto-Kinoshita, M., Blanco, A., Chen, S., Stutzer, A., Armache, K.J., Simon, M.D., Xu, C., Ali, M.*, et al.* (2014). A chromatin-dependent role of the fragile X mental retardation protein FMRP in the DNA damage response. Cell *157*, 869-881.

Ashley, C.T., Jr., Wilkinson, K.D., Reines, D., and Warren, S.T. (1993). FMR1 protein: conserved RNP family domains and selective RNA binding. Science *262*, 563-566.

Bear, M.F., Huber, K.M., and Warren, S.T. (2004). The mGluR theory of fragile X mental retardation. Trends Neurosci *27*, 370-377.

Brown, V., Jin, P., Ceman, S., Darnell, J.C., O'Donnell, W.T., Tenenbaum, S.A., Jin, X., Feng, Y., Wilkinson, K.D., Keene, J.D.*, et al.* (2001). Microarray identification of FMRP-associated brain mRNAs and altered mRNA translational profiles in fragile X syndrome. Cell *107*, 477-487.

Chen, C.L., Rappailles, A., Duquenne, L., Huvet, M., Guilbaud, G., Farinelli, L., Audit, B., d'Aubenton-Carafa, Y., Arneodo, A., Hyrien, O.*, et al.* (2010). Impact of replication timing on non-CpG and CpG substitution rates in mammalian genomes. Genome research *20*, 447-457.

Ciaccio, C., Fontana, L., Milani, D., Tabano, S., Miozzo, M., and Esposito, S. (2017). Fragile X syndrome: a review of clinical and molecular diagnoses. Ital J Pediatr *43*, 39.

Coffee, B., Zhang, F., Ceman, S., Warren, S.T., and Reines, D. (2002). Histone modifications depict an aberrantly heterochromatinized FMR1 gene in fragile x syndrome. American journal of human genetics *71*, 923-932.

Cristini, A., Groh, M., Kristiansen, M.S., and Gromak, N. (2018). RNA/DNA Hybrid Interactome Identifies DXH9 as a Molecular Player in Transcriptional Termination and R-Loop-Associated DNA Damage. Cell Rep *23*, 1891-1905.

Crosetto, N., Mitra, A., Silva, M.J., Bienko, M., Dojer, N., Wang, Q., Karaca, E., Chiarle, R., Skrzypczak, M., Ginalski, K.*, et al.* (2013). Nucleotide-resolution DNA double-strand break mapping by next-generation sequencing. Nature methods *10*, 361-365.

Daley, T., and Smith, A.D. (2013). Predicting the molecular complexity of sequencing libraries. Nature methods *10*, 325-327.

Darnell, J.C., Van Driesche, S.J., Zhang, C., Hung, K.Y., Mele, A., Fraser, C.E., Stone, E.F., Chen, C., Fak, J.J., Chi, S.W.*, et al.* (2011). FMRP stalls ribosomal translocation on mRNAs linked to synaptic function and autism. Cell *146*, 247-261.

De Boulle, K., Verkerk, A.J., Reyniers, E., Vits, L., Hendrickx, J., Van Roy, B., Van den Bos, F., de Graaff, E., Oostra, B.A., and Willems, P.J. (1993). A point mutation in the FMR-1 gene associated with fragile X mental retardation. Nature genetics *3*, 31-35.

de Leon, J. (2003). Glucuronidation enzymes, genes and psychiatry. Int J Neuropsychopharmacol *6*, 57-72.

Docampo, M., Olubu, A., Wang, X., Pasinetti, G., and Dixon, R.A. (2017). Glucuronidated Flavonoids in Neurological Protection: Structural Analysis and Approaches for Chemical and Biological Synthesis. J Agric Food Chem *65*, 7607-7623.

Dominguez-Sanchez, M.S., Barroso, S., Gomez-Gonzalez, B., Luna, R., and Aguilera, A. (2011). Genome instability and transcription elongation impairment in human cells depleted of THO/TREX. PLoS genetics *7*, e1002386.

Entian, K.D., Schuster, T., Hegemann, J.H., Becher, D., Feldmann, H., Guldener, U., Gotz, R., Hansen, M., Hollenberg, C.P., Jansen, G.*, et al.* (1999). Functional analysis of 150 deletion mutants in Saccharomyces cerevisiae by a systematic approach. Molecular & general genetics : MGG *262*, 683-702.

Favorov, A., Mularoni, L., Cope, L.M., Medvedeva, Y., Mironov, A.A., Makeev, V.J., and Wheelan, S.J. (2012). Exploring massive, genome scale datasets with the GenometriCorr package. PLoS computational biology *8*, e1002529.

Feng, Y., Absher, D., Eberhart, D.E., Brown, V., Malter, H.E., and Warren, S.T. (1997). FMRP associates with polyribosomes as an mRNP, and the I304N mutation of severe fragile X syndrome abolishes this association. Molecular cell *1*, 109-118.

Fu, Y.H., Kuhl, D.P., Pizzuti, A., Pieretti, M., Sutcliffe, J.S., Richards, S., Verkerk, A.J., Holden, J.J., Fenwick, R.G., Jr., Warren, S.T.*, et al.* (1991). Variation of the CGG repeat at the fragile X site results in genetic instability: resolution of the Sherman paradox. Cell *67*, 1047-1058.

Garcia-Rubio, M., Aguilera, P., Lafuente-Barquero, J., Ruiz, J.F., Simon, M.N., Geli, V., Rondon, A.G., and Aguilera, A. (2018). Yra1-bound RNA-DNA hybrids cause orientation-independent transcription-replication collisions and telomere instability. Genes & development *32*, 965-977.

Giulivi, C., Napoli, E., Tassone, F., Halmai, J., and Hagerman, R. (2016). Plasma Biomarkers for Monitoring Brain Pathophysiology in FMR1 Premutation Carriers. Front Mol Neurosci *9*, 71.

Glover, T.W., Berger, C., Coyle, J., and Echo, B. (1984). DNA polymerase alpha inhibition by aphidicolin induces gaps and breaks at common fragile sites in human chromosomes. Human genetics *67*, 136-142.

Greenblatt, E.J., and Spradling, A.C. (2018). Fragile X mental retardation 1 gene enhances the translation of large autism-related proteins. Science *361*, 709-712.

Hamperl, S., Bocek, M.J., Saldivar, J.C., Swigut, T., and Cimprich, K.A. (2017). Transcription-Replication Conflict Orientation Modulates R-Loop Levels and Activates Distinct DNA Damage Responses. Cell *170*, 774-786 e719.

Hansen, R.S., Thomas, S., Sandstrom, R., Canfield, T.K., Thurman, R.E., Weaver, M., Dorschner, M.O., Gartler, S.M., and Stamatoyannopoulos, J.A. (2010). Sequencing newly replicated DNA reveals widespread plasticity in human replication timing. Proceedings of the National Academy of Sciences of the United States of America *107*, 139-144.

Hayward, B.E., Zhou, Y., Kumari, D., and Usdin, K. (2016). A Set of Assays for the Comprehensive Analysis of FMR1 Alleles in the Fragile X-Related Disorders. The Journal of molecular diagnostics : JMD *18*, 762-774.

Heger, A., Webber, C., Goodson, M., Ponting, C.P., and Lunter, G. (2013). GAT: a simulation framework for testing the association of genomic intervals. Bioinformatics *29*, 2046-2048.

Hein, M.Y., Hubner, N.C., Poser, I., Cox, J., Nagaraj, N., Toyoda, Y., Gak, I.A., Weisswange, I., Mansfeld, J., Buchholz, F.*, et al.* (2015). A human interactome in three quantitative dimensions organized by stoichiometries and abundances. Cell *163*, 712-723.

Hellman, A., Rahat, A., Scherer, S.W., Darvasi, A., Tsui, L.C., and Kerem, B. (2000). Replication delay along FRA7H, a common fragile site on human chromosome 7, leads to chromosomal instability. Mol Cell Biol *20*, 4420-4427.

Hoffman, E.A., McCulley, A., Haarer, B., Arnak, R., and Feng, W. (2015). Break-seq reveals hydroxyurea-induced chromosome fragility as a result of unscheduled conflict between DNA replication and transcription. Genome research *25*, 402-412.

Kang, M.H., Das, J., Gurunathan, S., Park, H.W., Song, H., Park, C., and Kim, J.H. (2017). The cytotoxic effects of dimethyl sulfoxide in mouse preimplantation embryos: a mechanistic study. Theranostics *7*, 4735-4752.

Khandjian, E.W., Huot, M.E., Tremblay, S., Davidovic, L., Mazroui, R., and Bardoni, B. (2004). Biochemical evidence for the association of fragile X mental retardation protein with brain polyribosomal ribonucleoparticles. Proceedings of the National Academy of Sciences of the United States of America *101*, 13357-13362.

Korb, E., Herre, M., Zucker-Scharff, I., Gresack, J., Allis, C.D., and Darnell, R.B. (2017). Excess Translation of Epigenetic Regulators Contributes to Fragile X Syndrome and Is Alleviated by Brd4 Inhibition. Cell *170*, 1209-1223 e1220.

Krawczun, M.S., Jenkins, E.C., and Brown, W.T. (1985). Analysis of the fragile-X chromosome: localization and detection of the fragile site in high resolution preparations. Human genetics *69*, 209-211.

Kuwano, A., and Kajii, T. (1987). Synergistic effect of aphidicolin and ethanol on the induction of common fragile sites. Human genetics *75*, 75-78.

Landolfi, A., Troisi, J., Savanelli, M.C., Vitale, C., Barone, P., and Amboni, M. (2017). Bisphenol A glucuronidation in patients with Parkinson's disease. Neurotoxicology *63*, 90-96.

Le Beau, M.M., Rassool, F.V., Neilly, M.E., Espinosa, R., 3rd, Glover, T.W., Smith, D.I., and McKeithan, T.W. (1998). Replication of a common fragile site, FRA3B, occurs late in S phase and is delayed further upon induction: implications for the mechanism of fragile site induction. Human molecular genetics *7*, 755-761.

Li, H., Handsaker, B., Wysoker, A., Fennell, T., Ruan, J., Homer, N., Marth, G., Abecasis, G., and Durbin, R. (2009). The sequence alignment/map (SAM) format and SAMtools. Bioinformatics *25*, 2078-2079.

Li, Y., Stockton, M.E., Eisinger, B.E., Zhao, Y., Miller, J.L., Bhuiyan, I., Gao, Y., Wu, Z., Peng, J., and Zhao, X. (2018). Reducing histone acetylation rescues cognitive deficits in a mouse model of Fragile X syndrome. Nature communications *9*, 2494.

Liu, S.X., Athar, M., Lippai, I., Waldren, C., and Hei, T.K. (2001). Induction of oxyradicals by arsenic: implication for mechanism of genotoxicity. Proceedings of the National Academy of Sciences of the United States of America *98*, 1643-1648.

Murano, I., Kuwano, A., and Kajii, T. (1989). Fibroblast-specific common fragile sites induced by aphidicolin. Human genetics *83*, 45-48.

Nakamoto, M., Nalavadi, V., Epstein, M.P., Narayanan, U., Bassell, G.J., and Warren, S.T. (2007). Fragile X mental retardation protein deficiency leads to excessive mGluR5-dependent internalization of AMPA receptors. Proceedings of the National Academy of Sciences of the United States of America *104*, 15537-15542.

Niere, F., Wilkerson, J.R., and Huber, K.M. (2012). Evidence for a fragile X mental retardation protein-mediated translational switch in metabotropic glutamate receptor-triggered Arc translation and long-term depression. The Journal of neuroscience : the official journal of the Society for Neuroscience *32*, 5924-5936.

Palakodeti, A., Han, Y., Jiang, Y., and Le Beau, M.M. (2004). The role of late/slow replication of the FRA16D in common fragile site induction. Genes, chromosomes & cancer *39*, 71-76.

Perez-Pasten, R., Martinez-Galero, E., Garduno-Siciliano, L., Lara, I.C., and Cevallos, G.C. (2006). Effects of dimethylsulphoxide on mice arsenite-induced dysmorphogenesis in embryo culture and cytotoxicity in embryo cells. Toxicol Lett *161*, 167-173.

Pieretti, M., Zhang, F.P., Fu, Y.H., Warren, S.T., Oostra, B.A., Caskey, C.T., and Nelson, D.L. (1991). Absence of expression of the FMR-1 gene in fragile X syndrome. Cell *66*, 817-822.

Prado, F., and Aguilera, A. (2005). Impairment of replication fork progression mediates RNA polII transcription-associated recombination. The EMBO journal *24*, 1267-1276.

Quinlan, A.R., and Hall, I.M. (2010). BEDTools: a flexible suite of utilities for comparing genomic features. Bioinformatics *26*, 841-842.

Ross-Innes, C.S., Stark, R., Teschendorff, A.E., Holmes, K.A., Ali, H.R., Dunning, M.J., Brown, G.D., Gojis, O., Ellis, I.O., Green, A.R.*, et al.* (2012). Differential oestrogen receptor binding is associated with clinical outcome in breast cancer. Nature *481*, 389-393.

Sadowska-Bartosz, I., Paczka, A., Molon, M., and Bartosz, G. (2013). Dimethyl sulfoxide induces oxidative stress in the yeast Saccharomyces cerevisiae. FEMS Yeast Res *13*, 820-830.

Santoro, M.R., Bray, S.M., and Warren, S.T. (2012). Molecular mechanisms of fragile X syndrome: a twenty-year perspective. Annual review of pathology *7*, 219-245.

Sanz, L.A., Hartono, S.R., Lim, Y.W., Steyaert, S., Rajpurkar, A., Ginno, P.A., Xu, X., and Chedin, F. (2016). Prevalent, Dynamic, and Conserved R-Loop Structures Associate with Specific Epigenomic Signatures in Mammals. Molecular cell *63*, 167-178.

Savelyeva, L., and Brueckner, L.M. (2014). Molecular characterization of common fragile sites as a strategy to discover cancer susceptibility genes. Cellular and molecular life sciences : CMLS *71*, 4561-4575.

Sethna, F., Moon, C., and Wang, H. (2014). From FMRP function to potential therapies for fragile X syndrome. Neurochemical research *39*, 1016-1031.

Sheridan, S.D., Theriault, K.M., Reis, S.A., Zhou, F., Madison, J.M., Daheron, L., Loring, J.F., and Haggarty, S.J. (2011). Epigenetic characterization of the FMR1 gene and aberrant neurodevelopment in human induced pluripotent stem cell models of fragile X syndrome. PloS one *6*, e26203.

Siomi, H., Choi, M., Siomi, M.C., Nussbaum, R.L., and Dreyfuss, G. (1994). Essential role for KH domains in RNA binding: impaired RNA binding by a mutation in the KH domain of FMR1 that causes fragile X syndrome. Cell *77*, 33-39.

Verkerk, A.J., Pieretti, M., Sutcliffe, J.S., Fu, Y.H., Kuhl, D.P., Pizzuti, A., Reiner, O., Richards, S., Victoria, M.F., Zhang, F.P.*, et al.* (1991). Identification of a gene (FMR-1) containing a CGG repeat coincident with a breakpoint cluster region exhibiting length variation in fragile X syndrome. Cell *65*, 905-914.

Wang, L., Darling, J., Zhang, J.S., Huang, H., Liu, W., and Smith, D.I. (1999). Allele-specific late replication and fragility of the most active common fragile site, FRA3B. Human molecular genetics *8*, 431-437.

Wongsurawat, T., Jenjaroenpun, P., Kwoh, C.K., and Kuznetsov, V. (2012). Quantitative model of R-loop forming structures reveals a novel level of RNA-DNA interactome complexity. Nucleic acids research *40*, e16.

Yu, S., and Lemos, B. (2016). A Portrait of Ribosomal DNA Contacts with Hi-C Reveals 5S and 45S rDNA Anchoring Points in the Folded Human Genome. Genome biology and evolution *8*, 3545-3558.

SUPPLEMENTAL FIGURE LEGENDS

Figure S1. Break-seq data quality check. Break-seq sample read distribution of a *Pac*I site in the "proof-of-principle" experiment (**A**). (**B&C**) Break-seq library quality assessed by read classifications. "R1" and "R2", Read 1 an Read 2, respectively. Samples with the same treatment were merged to assess overall sequencing depth in (**C**). (**D**) Break-seq library complexity of FX and NM cells ("obs" and "exp" stand for observed and expected library complexities, respectively). Libraries from biological replicates for each treatment condition were merged for complexity measure.

Figure S2. Break-seq data analysis pipeline. (**A**) After Bowtie2 mapping, Break-seq data ("DMSO", "0.3 μM APH", and "0.03 μM APH") were normalized for copy number variation by whole genome DNA sequencing ("Total DNA"), for NM and FX cells, respectively (shown as an example for FX cells), during the peak calling step in MACS2. DSB peaks found in at least two replicate experiments for each strain/treatment combination were identified as "Consensus peaks" by DiffBind. Peaks from different APH treatments (0.03 μM and 0.3 μM) were then pooled into a single set of "Consensus peaks in APH", in contrast to the "Consensus peaks in DMSO" set. (**B**) The consensus peaks for each strain/treatment combination (as indicated) were compared with each other to identify overlaps and condition-specific peaks, ready for further comparison with genomic features such as RLFSs. (**C**) Comparison of DSBs between NM and FX cells for like treatments: Untreated, DMSO-treated, and APH-treated.

Figure S3. **Control experiments for RLFS-induced DNA breakage and recombination frequency (RF) in yeast.** (**A**) RF is dependent on transcriptional activation. (**B**) Insertions of RLFS elements from the human genome can further induce RF, specifically when inserted in the "sense" orientation with respect to transcription. (**C)** The RLFS-induced RF can be further enhanced by deletion of *rnh1*, the gene encoding for RNase H1. Note the change of scale on the Y-axis in (C). (**D**) Cells bearing a second plasmid, pRS313, which appeared to have little effect on RF, serve as control for the experiments in Fig. 3B. With the exception of (A), which employs an One-way ANOVA multiple comparison test, all statistical analysis employ the Two-way ANOVA multiple comparison test. Markers for statistical significance level are the same as in Fig. 3. (**E**) FMRP and FMRP-I304N show similar expression levels in yeast. Cells transformed with a plasmid with or without an RLFS in the LEU2 gene cassette, together with a plasmid with or without the CMV-driven and FLAG-tagged FMR1 or FMR1-I304N, were analyzed by Western blot using the anti-FLAG antibody. Actin served as a loading control.

Figure S4. FMRP chromatin-binding site analysis. (**A**) FMRP binding site distribution with respect to genes. (**B**) ChIP-qPCR validation of top FMRP binding substrates revealed by ChIP-seq. GAPDH served as control. Log10 values of the fold enrichment ratio (IP vs. input control) were plotted on the Y axis. (**C**) ChIP-seq enrichment ratios for fractions of FMRP chromatin binding sites with (pink) or without (blue) overlapping RLFSs. (**D**&**E**) Integrated Genome Viewer (IGV) screen shots of genes harboring FMRP chromatin-binding sites. (**D**) Learning and memory genes enriched for FMRP-binding sites. All except *SLC6A1* and *KRAS* also contain DSBs, albeit not within 1 kb distance to FMRP-binding sites, in FX cells. (**E**) Sixteen previously

validated mRNA substrates for FMRP, shown here as FMRP chromatin-binding sites and/or APH-induced DSBs in FX cells.

Figure S5. **FX-specific DSB formation in two phase I drug metabolic enzymes, CYP2C9 and CYP2C19.** IGV screenshots for CYP2C9 (**A**) and CYP2C19 (**B**)**.** (**C**) Representative Western blots of CYP2C9 protein expression with GAPDH as control and quantification using ratio of CYP2C9 to GAPDH derived from three biological replicates. Error bars denote standard deviation. P values that are < 0.05 from Two-way ANOVA test are shown.

Figure S6. Validation of observations made with FX lymphoblasts using FX fibroblasts (GM05848) and a sex- and age-matched control fibroblast cell line (GM00357). (**A&B**) Fibroblast cell line of an FX individual shows increased DNA damage compared to a control fibroblast cell line. Representative images of FX and NM cells under indicated treatment and stained for γH2A.X (**A**) and quantification of γH2A.X signals per nucleus (**B**) are shown. Forty-one to 43 nuclei per sample were analyzed and the error bars in (**B**) indicate standard deviation. One-way ANOVA test was performed: *, $p<0.05$; **, $p<0.01$; n.s., not significant. Scale bar, 10 μm. Two independent experiments were performed and one representative experiment shown here. (**C**) FX cells show increased RNA:DNA hybrid foci formation in the nucleus upon drug treatment detected by S9.6 antibody immunofluorescence. Nuclear boundary is marked by staining for Lamin A&C. Scale bar, 10 μm.

Figure S7. Genomic Association Test (GAT) for correlations between DSBs from the six indicated samples and the "APH breakome" mapped by BLESS. (**A**) Numbers of DSBs found associated with APH breakome signals in the indicated genomic regions. "Obs", observed number of DSBs; "Exp", expected number of DSBs. Log2 transformation of the fold enrichment values (ratios of observed to expected number of DSBs) are reported for the whole genome (**B**), the early replicating regions (**C**), and the late replicating regions (**D**). Those samples marked with an asterisk indicate p values ≤ 0.001.

SUPPLEMENTAL TABLES

Table S1. Proof-of principle Break-seq mapping of *Pac*I sites in DMSO- and (0.03 μM) APH-treated FX cells.

Cell line	Treatment	No. of DSB peaks	*Pac*I-positive	Concordance between *Pac*I-positives
FX	DMSO	84458	80819 (96%)	70630 (87%)
FX	APH*	87727	84975 (97%)	70592 (83%)

Table S2. Number of consensus DSB peaks (detected in at least 2 replicates) in all categories defined by strain/treatment/comparison combinations.

DSB category[1]	Number of DSBs
FX.APH	18473
FX.APH003	16796
FX.APH03	2112
FX.DMSO	9167
FX.NT	4149
FXdmso.FXaph.overlap	6177
FXdmso.FXaph.uniquetoFXaph	12296
FXdmso.FXaph.uniquetoFXdmso	2984
FXdmso.FXnt.overlap	322
FXdmso.FXnt.uniquetoFXdmso	8845
FXdmso.FXnt.uniquetoFXnt	3827
NM.APH	7002
NM.APH003	3506
NM.APH03	2161
NM.DMSO	3927
NM.NT	2111
NMdmso.NMaph.overlap	3209
NMdmso.NMaph.uniquetoNMaph	3792
NMdmso.NMaph.uniquetoNMdmso	714
NMdmso.NMnt.overlap	1651
NMdmso.NMnt.uniquetoNMdmso	2276
NMdmso.NMnt.uniquetoNMnt	458
FXdmso.NMdmso.overlap	644
FXdmso.NMdmso.uniquetoFXdmso	8523
FXdmso.NMdmso.uniquetoNMdmso	3283
FXnt.NMnt.overlap	1753
FXnt.NMnt.uniquetoFXnt	2396
FXnt.NMnt.uniquetoNMnt	358
FXaph.NMaph.overlap	4369
FXaph.NMaph.uniquetoFXaph	14104
FXaph.NMaph.uniquetoNMaph	2633

[1]Strain=FX, NM; Treatment=NT (untreated), DMSO, APH003 (0.03 μM APH), APH03 (0.3 μM APH), APH (composite of APH003 and APH03); Comparison=overlap (shared by two samples), uniquetoXXxx (unique to the sample indicated).

Table S3. Correlation between DSBs in various groups and 169222 computationally predicted RLFSs (Wongsurawat et al., 2012) and 108011 composite DRIP-seq signals merged from all DRIP-seq data sets (NT2 and K562) (Sanz et al., 2016). Note the merged DRIP-seq dataset has 6.6 times the coverage of the RLFSs.

DSB group	Query (RLFS or DRIP-seq)	Number of DSBs	Number of overlaps	Number of possible intervals	P value Left	P value Right	P value Two-tail	Ratio
FX.NT	RLFS	4149	133	2000047	2.34E-43	1	4.37E-43	0.358
FX.DMSO	RLFS	9167	1294	1702520	1	3.71E-37	6.24E-37	1.493
FX.APH	RLFS	18473	2323	1923061	1	1.25E-66	2.02E-66	1.498
NM.NT	RLFS	2111	129	1606572	7.31E-13	1	1.36E-12	0.552
NM.DMSO	RLFS	3927	659	1631798	1	1.22E-34	1.82E-34	1.746
NM.APH	RLFS	7002	554	1996033	0.045261	0.95877	0.089567	0.927
FX.NT	DRIP-seq	4149	526	642328	7.62E-14	1	1.54E-13	0.717
FX.DMSO	DRIP-seq	9167	2658	608194	1	1.07E-155	1.55E-155	1.914
FX.APH	DRIP-seq	18473	4137	634175	1	1.36E-80	2.21E-80	1.422
NM.NT	DRIP-seq	2111	389	595489	0.64755	0.37359	0.73422	1.02
NM.DMSO	DRIP-seq	3927	1229	598921	1	2.21E-90	2.98E-90	2.083
NM.APH	DRIP-seq	7002	1326	641914	1	1.57E-06	2.93E-06	1.157

P values were calculated using bedtools Fisher's Exact Test. "NT", untreated.

Table S4. Number of genes containing DSBs in FX cells that overlap RLFSs or DRIP-seq signals.

DSB Group	Total DSBs	Genes containing DSBs*	Genes containing DSBs that overlap RLFSs*	Genes containing DSBs that overlap DRIP-seq signals*
FXdmso.FXaph.overlap	6177 (28.8%)	4121 (27.8%)	894 (33.1%)	2364 (37.8%)
FXdmso.FXaph.uniquetoFXaph	12296 (57.3%)	8715 (58.8%)	1427 (52.9%)	3113 (49.8%)
FXdmso.FXaph.uniquetoFXdmso	2984 (13.9%)	1990 (13.4%)	378 (14.0%)	778 (12.4%)
FXdmso.FXaph.total	21457 (100%)	14826 (100%)	2699 (100%)	6255 (100%)
NMdmso.NMaph.overlap	3209 (41.6%)	2484 (41.4%)	523 (50.7%)	1240 (41.3%)
NMdmso.NMaph.uniquetoNMaph	3792 (49.2%)	2524 (42.1%)	153 (14.8%)	718 (23.9%)
NMdmso.NMaph.uniquetoNMdmso	714 (9.3%)	990 (16.5%)	356 (34.5%)	1042 (34.7%)
NMdmso.NMaph.total	7715 (100%)	5998 (100%)	1032 (100%)	3000 (100%)

* Percentages in parentheses indicate the percentage of DSBs or genes in each of the three categories (e.g., XX.XX.overlap, XX.XX.uniquetoXXaph, and XX.XX.uniquetoXXdmso) over the sum of the three categories.

Table S5. Select top Gene Ontology terms ($p < 0.001$) for "Biological pathways" associated with DSBs in the indicated groups.

DSB Group	Biological pathway	P value	# of genes
FX_UNTREATED	neuron projection development	1.12E-05	100
	nervous system development	2.08E-05	214
	regulation of cell morphogenesis	2.08E-05	66
	synapse organization	5.29E-05	40
	regulation of neuron projection development	6.25E-05	58
	neuron development	8.09E-05	109
	neuron cell-cell adhesion	0.00015	9
	neuron projection morphogenesis	0.00018	70
	ion transmembrane transport	0.00025	107
	inorganic ion transmembrane transport	0.00048	85
FX_DMSO	cell projection organization	0.00030	187
	localization	0.00030	717
	cell part morphogenesis	0.00050	131
	inorganic ion transmembrane transport	0.00052	118
	neuron development	0.00075	146
	cell projection morphogenesis	0.00086	126
FX_APH	positive regulation of GTPase activity	6.76E-06	180
	regulation of cell morphogenesis	7.35E-06	139
	nervous system development	1.15E-05	504
	regulation of cell projection organization	4.09E-05	152
	neuron projection development	5.56E-05	213
	regulation of neuron projection development	9.09E-05	119
	cell adhesion	0.000107	405
	chemical synaptic transmission	0.000107	163
	movement of cell or subcellular component	0.000199	415
	cell projection assembly	0.000212	113
	vesicle-mediated transport	0.000347	343
	synaptic vesicle localization	0.000569	46
	microtubule-based process	0.000596	160
	synaptic vesicle cycle	0.000681	41
	dendrite development	0.000733	63
	cytoskeleton organization	0.000784	271
NM_UNTREATED	None		
NM_DMSO	None		
NM_APH	regulation of cell projection organization	2.20E-06	108
	regulation of cell morphogenesis	1.56E-05	94
	cell projection organization	3.97E-05	201
	regulation of neuron projection development	0.000217	80
	neuron projection development	0.000559	135
	neuron development	0.000559	154
	nervous system development	0.000646	305
	cellular component morphogenesis	0.000646	186
FX_DMSO_RLFS_overlap	flavonoid glucuronidation	0.000136	8
	cellular glucuronidation	0.000208	8
	uronic acid metabolic process	0.000499	8
	flavonoid metabolic process	0.000499	8
	flavonoid biosynthetic process	0.000499	7
	glucuronate metabolic process	0.000499	8
FX_APH_RLFS_overlap	single-organism membrane organization	0.001285	84

Table S6. Primers for ChIP-qPCR and RT-qPCR.

Gene name	Primer Name	Sequence
ANK1	ANK1-F	5'- CTTAGAGGGTGAGGCAGACG-3'
	ANK1-R	5'- ACATCCAGGTGTTTGGCTTC-3'
ASTN2	ASTN2-F	5'-GTGCTGAGCTTCACACGGTA-3'
	ASTN2-R	5'-AGAGCTGCAGGGTGAACAAT-3'
CLNK1	CLNK-F	5'-TGTCCCATCTCCTCAGGAAC-3'
	CLNK-R	5'-GCCCAATTCTGCCTCTTTCT-3'
DLG1	DLG1-F	5'-AGCTTTTCCTTGGAGTGGGTA-3'
	DLG1-R	5'-ATACTTGTGCGGGGGAAGAG-3'
GAPDH	GAPDH-F	5'-GACCTGACCTGCCGTCTAGA-3'
	GAPDH-R	5'-ACCTGGTGCTCAGTGTAGCC-3'

Table S7. (separate file)

487 genes that contain co-localized FMRP binding sites and RLFSs (within 1 kb of each other). The table headers are largely self-evident. Columns A through I follow the MACS peak identification output file format (https://github.com/taoliu/MACS#call-peaks). The 487 unique genes are derived from column N ("symbol_g") for those entries for which the value in column AH ("RLFS_1kupdown") is greater than 0.
File attachment: Supplemental_Table_S7.txt

Movie S1. (separate file)

Movie for a cell showing co-localization of FMRP and RNA:DNA hybrid.

File attachment: Supplemental_Movie_S1.AVI

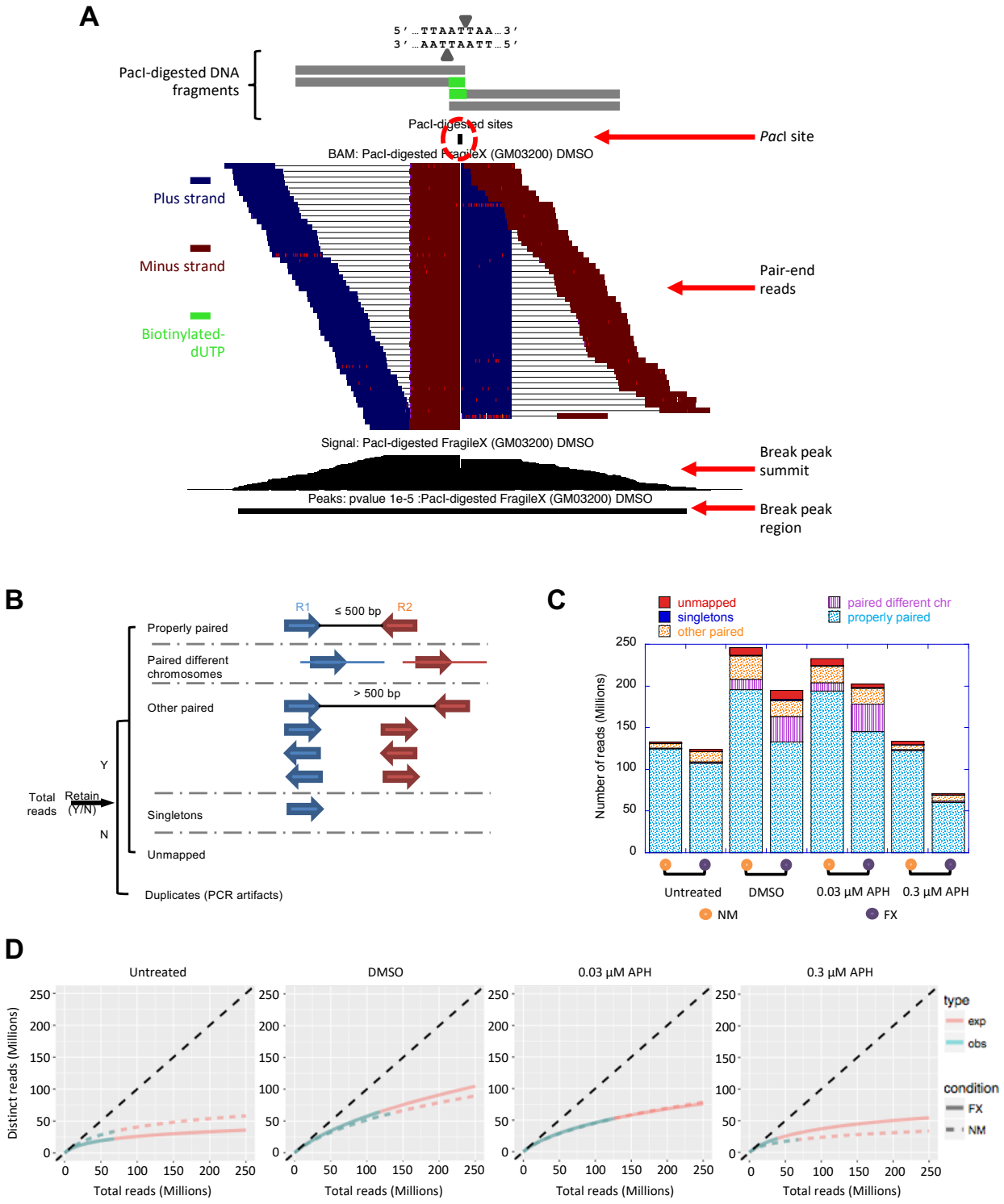

Figure S1. Break-seq data quality check. Break-seq sample read distribution of a *Pac*I site in the "proof-of-principle" experiment (**A**). (**B&C**) Break-seq library quality assessed by read classifications. "R1" and "R2", Read 1 an Read 2, respectively. Samples with the same treatment were merged to assess overall sequencing depth in (**C**). (**D**) Break-seq library complexity of FX and NM cells ("obs" and "exp" stand for observed and expected library complexities, respectively). Libraries from biological replicates for each treatment condition were merged for complexity measure.

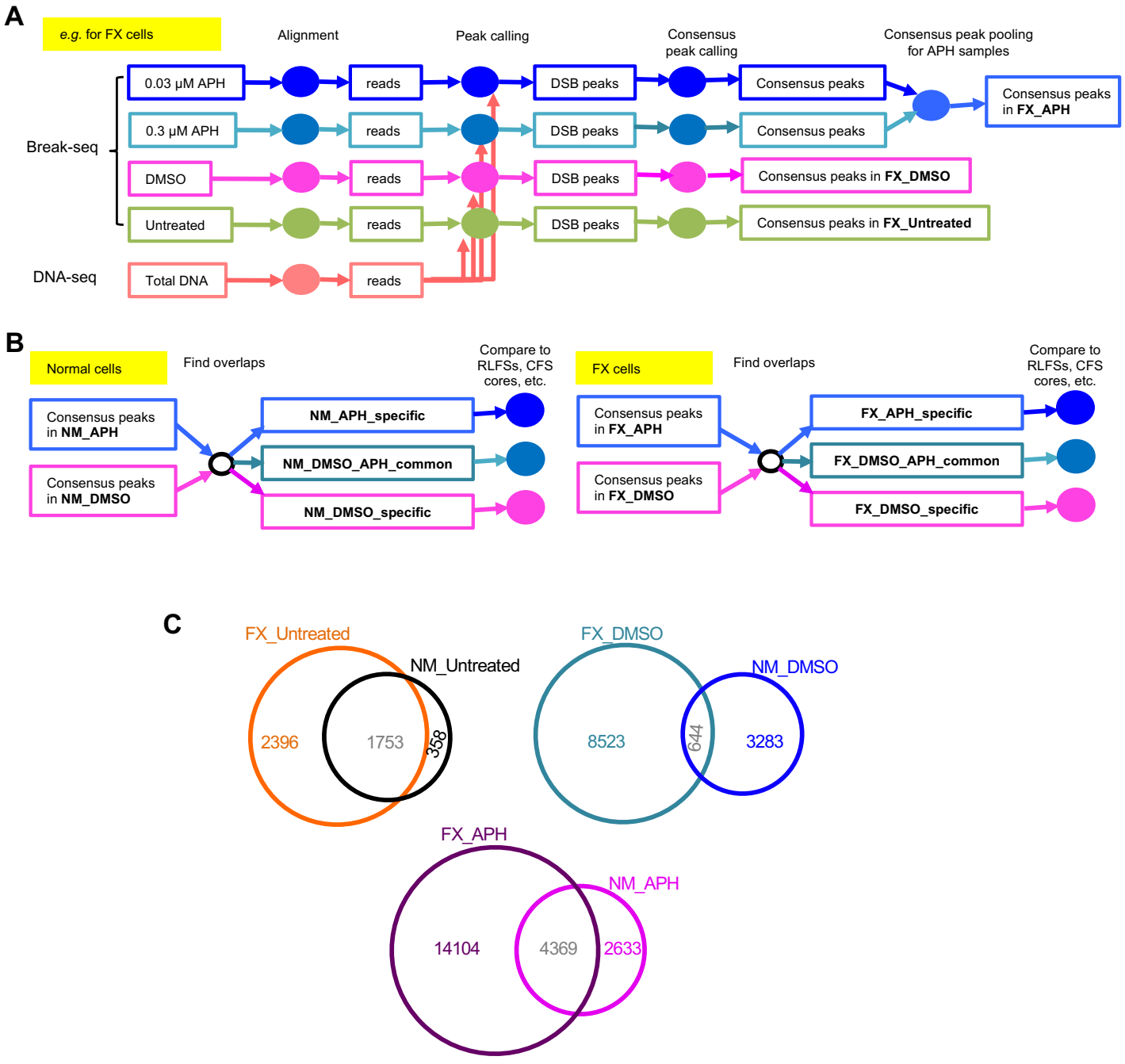

Figure S2. Break-seq data analysis pipeline. (**A**) After Bowtie2 mapping, Break-seq data ("DMSO", "0.3 μM APH", and "0.03 μM APH") were normalized for copy number variation by whole genome DNA sequencing ("Total DNA"), for NM and FX cells, respectively (shown as an example for FX cells), during the peak calling step in MACS2. DSB peaks found in at least two replicate experiments for each strain/treatment combination were identified as "Consensus peaks" by DiffBind. Peaks from different APH treatments (0.03 μM and 0.3 μM) were then pooled into a single set of "Consensus peaks in APH", in contrast to the "Consensus peaks in DMSO" set. (**B**) The consensus peaks for each strain/treatment combination (as indicated) were compared with each other to identify overlaps and condition-specific peaks, ready for further comparison with genomic features such as RLFSs. (**C**) Comparison of DSBs between NM and FX cells for like treatments: Untreated, DMSO-treated, and APH-treated.

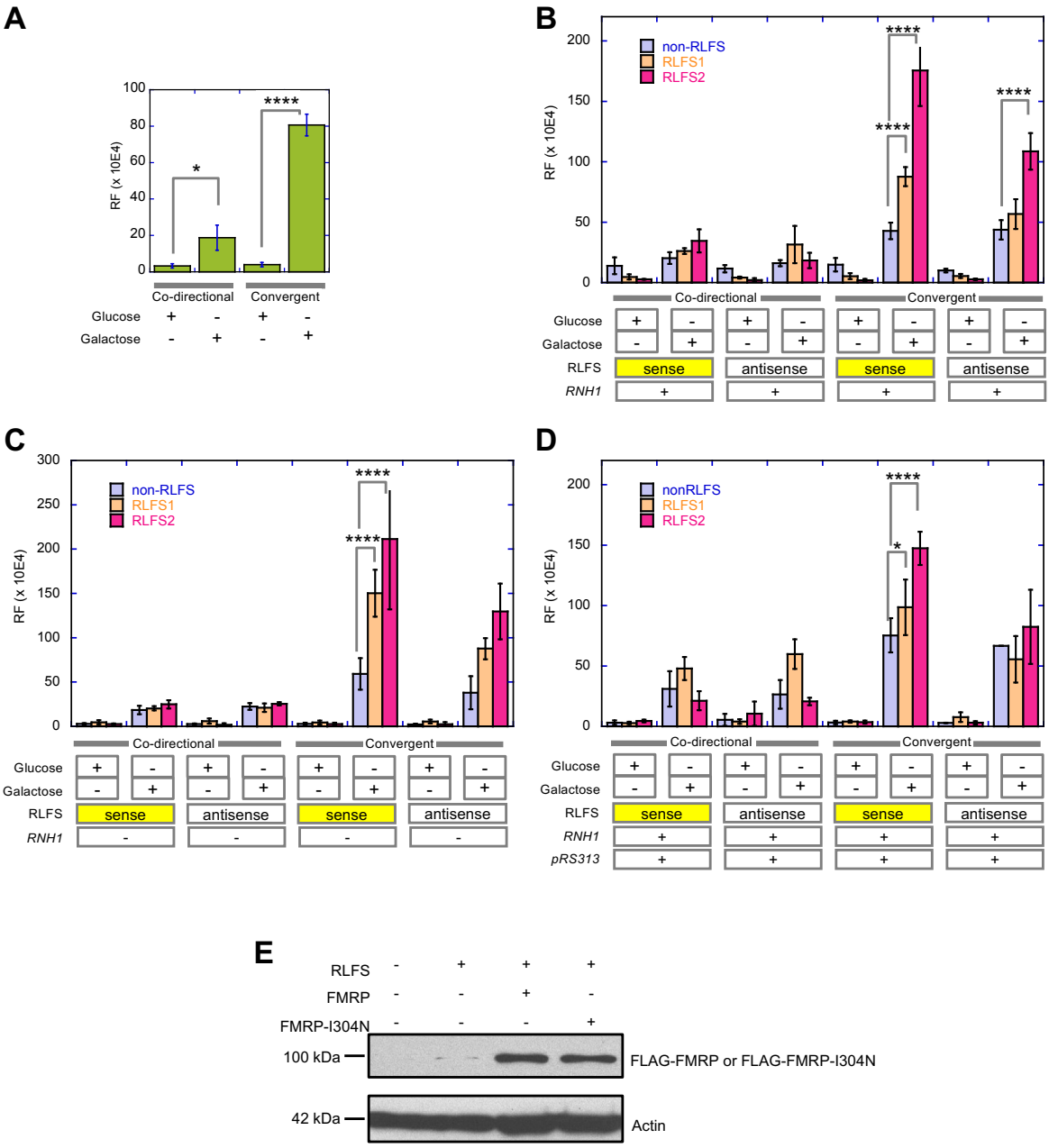

Figure S3. **Control experiments for RLFS-induced DNA breakage and recombination frequency (RF) in yeast.** (**A**) RF is dependent on transcriptional activation. (**B**) Insertions of RLFS elements from the human genome can further induce RF, specifically when inserted in the "sense" orientation with respect to transcription. (**C**) The RLFS-induced RF can be further enhanced by deletion of *rnh1*, the gene encoding for RNase H1. Note the change of scale on the Y-axis in (C). (**D**) Cells bearing a second plasmid, pRS313, which appeared to have little effect on RF, serve as control for the experiments in Fig. 3B. With the exception of (A), which employs an One-way ANOVA multiple comparison test, all statistical analysis employ the Two-way ANOVA multiple comparison test. Markers for statistical significance level are the same as in Fig. 3. (**E**) FMRP and FMRP-I304N show similar expression levels in yeast. Cells transformed with a plasmid with or without an RLFS in the LEU2 gene cassette, together with a plasmid with or without the CMV-driven and FLAG-tagged FMR1 or FMR1-I304N, were analyzed by Western blot using the anti-FLAG antibody. Actin served as a loading control.

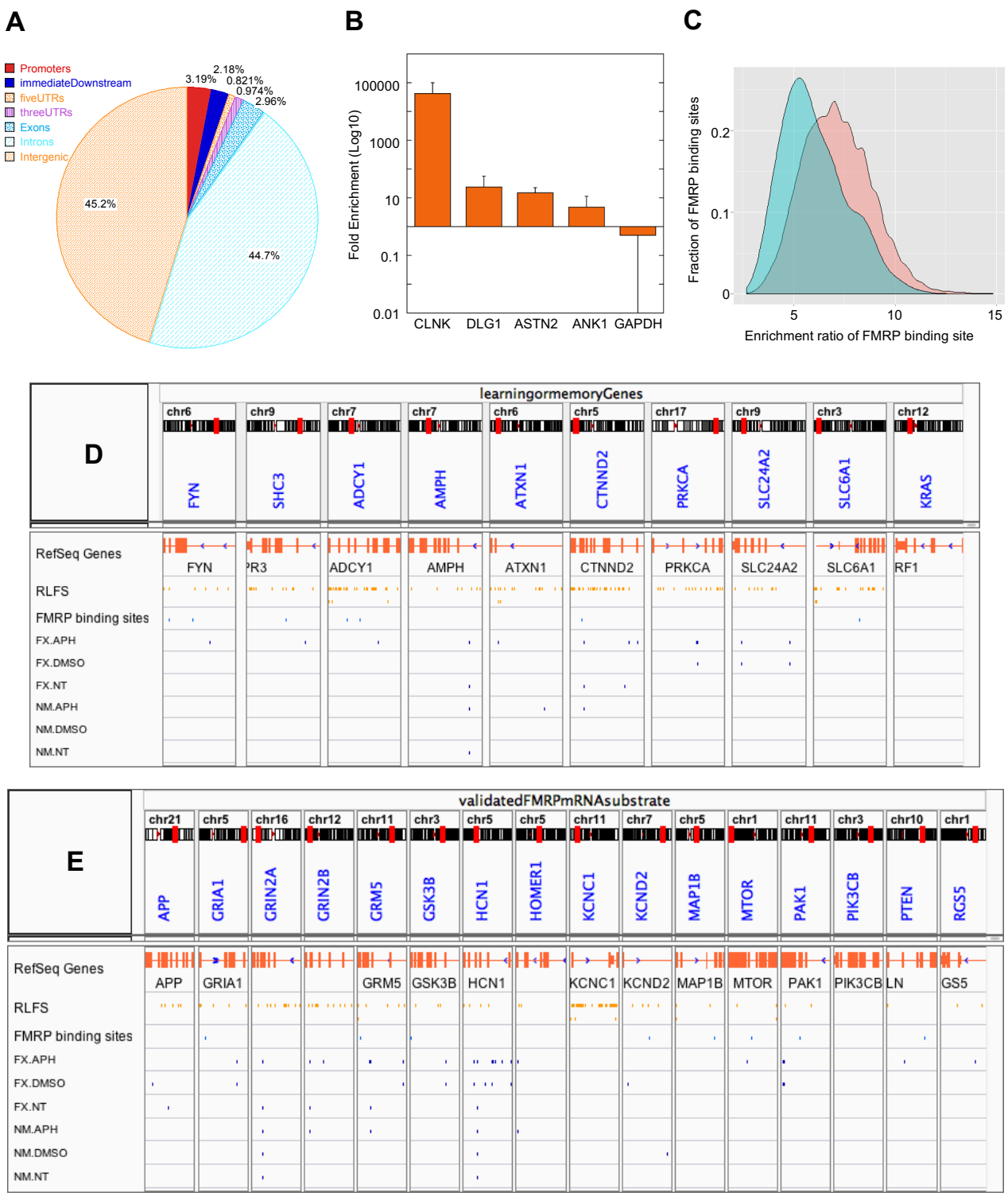

Figure S4. FMRP chromatin-binding site analysis. (**A**) FMRP binding site distribution with respect to genes. (**B**) ChIP-qPCR validation of top FMRP binding substrates revealed by ChIP-seq. GAPDH served as control. Log10 values of the fold enrichment ratio (IP vs. input control) were plotted on the Y axis. (**C**) ChIP-seq enrichment ratios for fractions of FMRP chromatin binding sites with (pink) or without (blue) overlapping RLFSs. (**D&E**) Integrated Genome Viewer (IGV) screen shots of genes harboring FMRP chromatin-binding sites. (**D**) Learning and memory genes enriched for FMRP-binding sites. All except *SLC6A1* and *KRAS* also contain DSBs, albeit not within 1 kb distance to FMRP-binding sites, in FX cells. (**E**) Sixteen previously validated mRNA substrates for FMRP, shown here as FMRP chromatin-binding sites and/or APH-induced DSBs in FX cells.

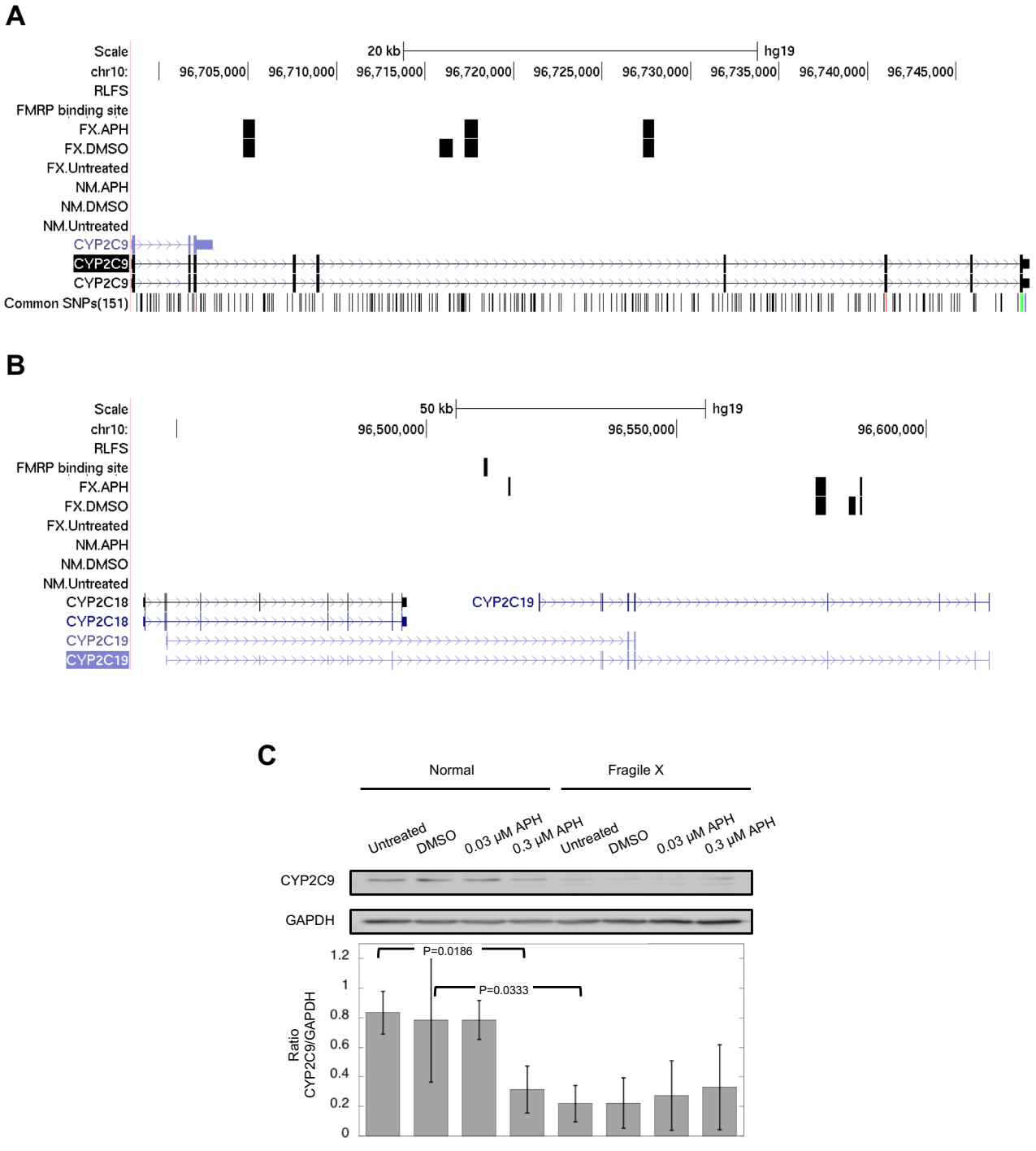

Figure S5. **FX-specific DSB formation in two phase I drug metabolic enzymes, CYP2C9 and CYP2C19.** IGV screenshots for CYP2C9 (**A**) and CYP2C19 (**B**). (**C**) Representative Western blots of CYP2C9 protein expression with GAPDH as control and quantification using ratio of CYP2C9 to GAPDH derived from three biological replicates. Error bars denote standard deviation. P values that are < 0.05 from Two-way ANOVA test are shown.

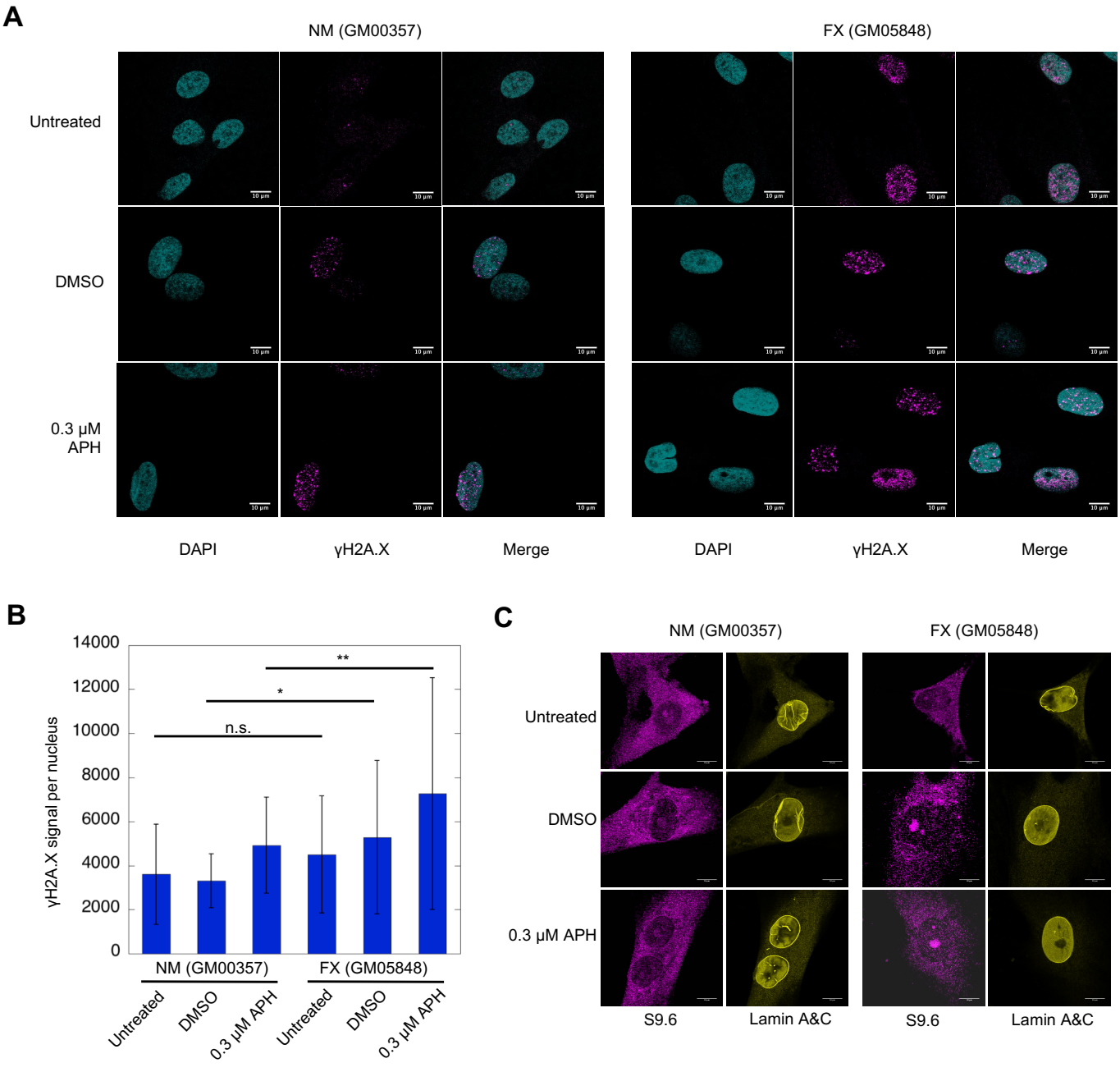

Figure S6. Validation of observations made with FX lymphoblasts using FX fibroblasts (GM05848) and a sex- and age-matched control fibroblast cell line (GM00357). (**A&B**) Fibroblast cell line of an FX individual shows increased DNA damage compared to a control fibroblast cell line. Representative images of FX and NM cells under indicated treatment and stained for γH2A.X (**A**) and quantification of γH2A.X signals per nucleus (**B**) are shown. Forty-one to 43 nuclei per sample were analyzed and the error bars in (**B**) indicate standard deviation. One-way ANOVA test was performed: *, $p<0.05$; **, $p<0.01$; n.s., not significant. Scale bar, 10 μm. Two independent experiments were performed and one representative experiment shown here. (**C**) FX cells show increased RNA:DNA hybrid foci formation in the nucleus upon drug treatment detected by S9.6 antibody immunofluorescence. Nuclear boundary is marked by staining for Lamin A&C. Scale bar, 10 μm.

A

Sample	Whole genome (Obs/Exp)	Early Replicating (Obs/Exp)	Late Replicating (Obs/Exp)
NM.Untreated	141/106	33/26	100/85
NM_DMSO	337/195	44/56	265/143
NM_APH	568/333	75/79	456/273
FX_Untreated	226/200	49/51	171/162
FX_DMSO	781/427	155/106	566/332
FX_APH	1219/849	283/221	854/635

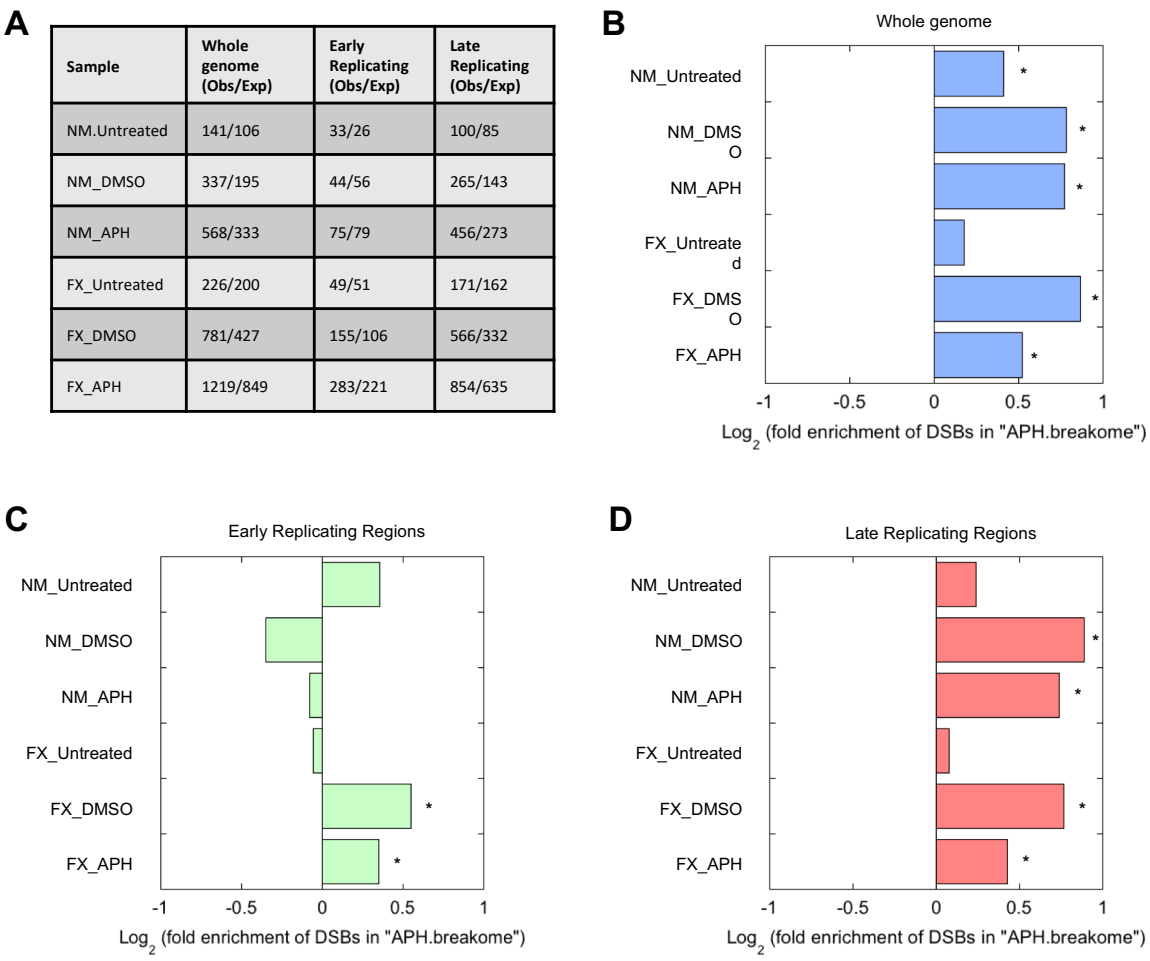

Figure S7. Genomic Association Test (GAT) for correlations between DSBs from the six indicated samples and the "APH breakome" mapped by BLESS. (**A**) Numbers of DSBs found associated with APH breakome signals in the indicated genomic regions. "Obs", observed number of DSBs; "Exp", expected number of DSBs. Log2 transformation of the fold enrichment values (ratios of observed to expected number of DSBs) are reported for the whole genome (**B**), the early replicating regions (**C**), and the late replicating regions (**D**). Those samples marked with an asterisk indicate p values ≤ 0.001.